Photochemistry and Spectral Characterization of Temperate and Gas-rich Exoplanets

Renyu Hu[1,2,3,4]
[1] Jet Propulsion Laboratory, California Institute of Technology, Pasadena, CA 91109, USA; renyu.hu@jpl.nasa.gov
[2] Division of Geological and Planetary Sciences, California Institute of Technology, Pasadena, CA 91125, USA

Abstract

Exoplanets that receive stellar irradiance approximately equal to Earth's or less have been discovered and many are suitable for spectral characterization. Here, we focus on the temperate planets that have massive H_2-dominated atmospheres, and trace the chemical reactions and transport following the photodissociation of H_2O, CH_4, NH_3, and H_2S, with K2-18 b, PH2 b, and Kepler-167 e representing temperate/cold planets around M and G/K stars. We find that NH_3 is likely depleted by photodissociation to the cloud deck on planets around G/K stars but remains intact in the middle atmosphere of planets around M stars. A common phenomenon on temperate planets is that the photodissociation of NH_3 in the presence of CH_4 results in HCN as the main photochemical product. The photodissociation of CH_4 together with H_2O leads to CO and CO_2, and the synthesis of hydrocarbon is suppressed. Temperate planets with a supersolar atmospheric metallicity and appreciable internal heat may have additional CO and CO_2 from the interior and less NH_3, and thus less HCN. Our models of K2-18 b can explain the transmission spectrum measured by the Hubble Space Telescope, and indicate that future observations in 0.5–5.0 μm wavelength range would provide the sensitivity to detect the equilibrium gases CH_4, H_2O, and NH_3, the photochemical gas HCN, as well as CO_2 in some cases. Temperate and H_2-rich exoplanets are thus laboratories of atmospheric chemistry that operate in regimes not found in the solar system, and spectral characterization of these planets in transit or reflected starlight promises to greatly expand the types of molecules detected in exoplanet atmospheres.

Unified Astronomy Thesaurus concepts: Exoplanet atmospheres (487); Extrasolar gaseous planets (2172); Extrasolar ice giants (2024); Mini Neptunes (1063); Habitable zone (696); Transmission spectroscopy (2133)

1. Introduction

The era of characterizing temperate exoplanets has begun. Kepler, K2, and TESS missions have found a few tens of exoplanets cold enough for water to condense in their atmospheres in transiting orbits (from the NASA Exoplanet Archive). Another handful of temperate planets may be confirmed in the next few years with ongoing validation and follow-up of TESS planet candidates (Barclay et al. 2018). A small subset of these planets has been observed by the Hubble Space Telescope (HST) for transmission spectra (De Wit et al. 2018; Zhang et al. 2018; Benneke et al. 2019; Tsiaras et al. 2019). For example, a transmission spectrum obtained by the HST at 1.1–1.7 μm of the temperate sub-Neptune K2-18 b shows spectral features (Benneke et al. 2019; Tsiaras et al. 2019), and the spectrum indicates that the planet hosts an atmosphere dominated by H_2, and which includes H_2O and/or CH_4 (Benneke et al. 2019; Madhusudhan et al. 2020; Blain et al. 2021). TOI-1231 b is another temperate planet suitable for atmospheric studies with transits (Burt et al. 2021). With >7 times more collecting area and infrared instruments, the James Webb Space Telescope (JWST) will be capable of providing a more detailed look into the atmospheres of these temperate exoplanets (Beichman et al. 2014).

We refer to the exoplanets that receive stellar irradiance approximately equal to Earth's as "temperate exoplanets" and to those that receive less irradiance by approximately an order of magnitude as "cold exoplanets" in this paper. Temperate and cold exoplanets include both giant planets and small planets and potentially have diverse atmospheric compositions. Giant planets (Jupiters and Neptunes) have massive H_2/He envelopes (e.g., Burrows et al. 2001), and small planets (mini-Neptunes, super-Earths, and Earth-sized planets) can have H_2/He atmospheres with variable abundances of heavy elements, steam atmospheres mostly made of water, or secondary atmospheres from outgassing (e.g., Fortney et al. 2013; Moses et al. 2013; Hu & Seager 2014).

In this paper, we focus on temperate/cold and gas-rich exoplanets, which include temperate/cold giant planets and mini-Neptunes. We assume that the atmospheres are H_2/He-dominated and massive enough for thermochemical equilibrium to prevail at at the bottom. This condition determines that the dominant O, C, N, and S species should be H_2O, CH_4, NH_3, and H_2S on temperate and cold planets in most cases (e.g., Fegley & Lodders 1996; Burrows & Sharp 1999; Heng & Tsai 2016; Woitke et al. 2021). Thermochemical equilibrium may also produce N_2 as the dominant N species and a substantial abundance of CO and CO_2 if the planet has a hot interior (e.g., Fortney et al. 2020). On temperate and cold planets, H_2O can condense to form a cloud, and the above-cloud H_2O is partially depleted as a result (e.g., Morley et al. 2014; Hu 2019; Charnay et al. 2021). Cold planets may additionally have NH_4SH (from the combination reaction between NH_3 and H_2S) and NH_3 condensed to form clouds (e.g., Lewis 1969; Atreya et al. 1999). This paper primarily concerns the photochemical processes above the clouds, with H_2O, CH_4, NH_3, and H_2S as the feedstock.

Past work on the atmospheric photochemistry of low-temperature and gas-rich planets in the exoplanet context is rare. Moses et al. (2016) studied the thermochemistry and photochemistry in directly imaged young giant planets, and discussed the photochemical production of CO_2 and HCN in

---

their atmospheres. Zahnle et al. (2016) showed that sulfur haze can form photochemically in the young Jupiter 51 Eri b, and the level of the sulfur haze would move upward in the atmosphere when the eddy diffusion coefficient increases. Gao et al. (2017) further modeled the effect of the sulfur haze on the reflected starlight spectra of widely separated giant planets. Here, we systematically study the atmospheric photochemistry of H_2O, CH_4, NH_3, and H_2S in low-temperature exoplanetary atmospheres and model the abundance of the photochemical gases to guide the future observations of temperate/cold and gas-rich exoplanets.

The paper is organized as follows: Section 2 describes the models used in this study; Section 3 presents the results in terms of the main behaviors of atmospheric chemistry, key photochemical mechanisms, and the corresponding spectral features in transmission and reflected starlight; Section 4 discusses the prospect to detect photochemical gases in temperate and gas-rich exoplanets and potential areas of further development; and Section 5 summarizes the key findings of this study.

2. Methods

2.1. Atmospheric Structure Model

We use the atmospheric structure and cloud formation model in Hu (2019) to simulate the pressure–temperature profile and potential gas depletion by condensation in temperate and cold exoplanets.

We have updated the model with a routine to compute the condensation of the NH_4SH cloud, in a way similar to that of the equilibrium cloud condensation model of Atreya & Romani (1985). In short, we compare the products of the partial pressure of NH_3 and H_2S with the equilibrium constant of the reaction that produces an NH_4SH solid (Lewis 1969), and partition the NH_3 and H_2S in excess to form the NH_4SH solid cloud in each atmospheric layer. We have verified that the resulting NH_4SH cloud density and pressure level is consistent with those of the previously published models when applied to a Jupiter-like planet (e.g., Atreya et al. 1999).

Another update is that the model now traces the concentration of NH_3 in liquid-water cloud droplets when applicable. The model of Hu (2019) has included the dissolution of NH_3 in the liquid-water droplets. By additionally tracing the concentration of NH_3 in droplets, we have now taken into account the non-ideal effects when the NH_3 solution is non-dilute. When the mass ratio between NH_3 and H_2O in the droplet is >0.05, we replace Henry's law with the vapor pressure of NH_3 in equilibrium with the solution (Perry & Green 2007). The latter merges the solubility in the Henry's law regime to that in the Raoult's law regime smoothly. We also apply the vapor pressure of H_2O in equilibrium with the solution, which can be substantially smaller than that with pure water when the solution is non-dilute (i.e., Raoult's law). While the impact of these processes on the overall atmospheric composition of the planets studied in this paper—planets warmer than Jupiter—is small, these processes may control the mixing ratio of H_2O and NH_3 in the atmospheres of even colder planets (De Pater et al. 1989; Romani et al. 1989).

2.2. Atmospheric Photochemical Model

We use the general-purpose photochemical model in Hu et al. (2012, 2013) to simulate the photochemical products in the middle atmospheres of temperate and cold exoplanets. The photochemical model includes a carbon chemistry network and a nitrogen chemistry network and their interactions (Hu et al. 2012). The photochemical model also includes a sulfur chemistry network and calculates the formation of H_2SO_4 and S_8 aerosols when applicable (Hu et al. 2013).

We have made several updates to the original reaction network (Hu et al. 2012), and they are listed in Table 1. We have checked the main reactions that produce, remove, and exchange C_1 and C_2 hydrocarbons in the Jovian atmosphere (Gladstone et al. 1996; Moses et al. 2005) and updated rate constants when more recent values in the relevant temperature range are available in the NIST Chemical Kinetics Database. We have added low-pressure or high-pressure rate constants for three-body reactions if any of them were missing in the original reaction rate list. Certain reactions important for the hydrocarbon chemistry do not have a directly usable rate constant expression in the NIST database; rather, their rates are fitted on experimental data or estimated by Moses et al. (2005). We have also added several reactions that involve NH because it may be produced by NH_3 photodissociation, and updated the rate constant of an important reaction $NH_2 + CH_4 \rightarrow NH_3 + CH_3$ to the latest calculated value. Lastly, we have removed two reactions that were incorrectly included, $CH_4 + C_2H_2 \rightarrow C_2H_3 + CH_3$ and $C_2H_6 + C_2H_2 \rightarrow C_2H_3 + C_2H_5$, because the reactant should have been $CH_2 = C$.

The photochemical model is applied to the "stratosphere" of the atmosphere, where the "tropopause" is defined as the pressure level at which the temperature profile becomes adiabatic. We define the lower boundary of the model as the pressure level 10-fold greater than the tropopause pressure, and thus include a section of the "troposphere" in the model. These choices are customary in photochemical studies of giant planets' atmospheres (e.g., Gladstone et al. 1996), and reasonable because the photochemical products in the stratosphere (and above the condensation clouds) are the objective of the study. Including a section of the troposphere makes sure that the results do not strongly depend on the lower boundary conditions assumed.

We apply fixed mixing ratios as the lower boundary conditions for H_2, He, H_2O, CH_4, NH_3, and when applicable, H_2S according to the assumed elemental abundance. When interior sources of CO, CO_2, and N_2 are included in some scenarios (see Section 2.4 for details), fixed mixing ratios are also applied to these gases at the lower boundary. We assume that all other species can move across the lower boundary (i.e., dry deposition when the lower boundary is a surface in terrestrial planet models) at a velocity of K_{zz}/H, where K_{zz} is the eddy diffusion coefficient and H is the scale height. This velocity is the upper limit of the true diffusion velocity, which could be damped by the gradient of the mixing ratio (Gladstone et al. 1996); however, the velocity only matters for long-lived species (e.g., C_2H_6 in Jupiter). Our choice of lower boundary conditions thus results in conservative estimates of the abundance of long-lived photochemical gases.

The upper boundary is assumed to be at 10^{-4} Pa, i.e., small enough so that the peaks of photodissociation of all species are well within the modeled atmosphere. Following Gladstone et al. (1996), we assume a zero-flux boundary condition for all species except for H, for which we include a downward flux of 4×10^9 cm^{-2} s^{-1} (Waite et al. 1983) to account for ionospheric processes that produce H. This influx of H was calculated for

Table 1
Reactions and Rate Constants Updated with Respect to Hu et al. (2012)

Reaction	Rate	Reason for Update	Source
$H + C_2H_3 \rightarrow C_2H_2 + H_2$	$1.2 \times 10^{-12}T^{0.5}$	Revise rate	Moses et al. (2005)
$H + C_2H_4 \rightarrow C_2H_3 + H_2$	$5.0 \times 10^{-12}(T/298)^{1.93}\exp(-6520/T)$	Revise rate	NIST
$H + C_2H_5 \rightarrow 2\,CH_3$	1.25×10^{-10}	Revise rate	NIST
$CH + CH_4 \rightarrow C_2H_4 + H$	$9.1 \times 10^{-11}(T/298)^{-0.9}\ (T > 295\ K)$	Revise rate	NIST
	$1.06 \times 10^{-10}(T/298)^{-1.04}\exp(-36/T)\ (T \leqslant 295\ K)$		
$CH_3 + H_2 \rightarrow CH_4 + H$	$2.31 \times 10^{-14}(T/298)^{2.24}\exp(-3220.0/T)$	Revise rate	NIST
$C_2H + CH_4 \rightarrow C_2H_2 + CH_3$	$1.2 \times 10^{-11}\exp(-490.7/T)$	Revise rate	NIST
$C_2H + C_2H_6 \rightarrow C_2H_2 + C_2H_5$	$2.58 \times 10^{-11}(T/298)^{0.54}\exp(180/T)$	Revise rate	NIST
$C_2H_3 + H_2 \rightarrow C_2H_4 + H$	$3.39 \times 10^{-14}(T/298)^{2.56}\exp(-2530.5/T)$	Revise rate	NIST
$C_2H_3 + C_2H_5 \rightarrow 2C_2H_4$	8.0×10^{-13}	Revise rate	Moses et al. (2005)
$C_2H_3 + C_2H_5 \rightarrow C_2H_2 + C_2H_6$	8.0×10^{-13}	Revise rate	Moses et al. (2005)
$C_2H_5 + C_2H_5 \rightarrow C_2H_6 + C_2H_4$	2.4×10^{-12}	Revise rate	NIST
$NH + NH \rightarrow N_2H_2$	$8.47 \times 10^{-11}(T/298)^{-0.04}\exp(80.6/T)$	Add reaction	NIST
$NH + NH_2 \rightarrow N_2H_2 + H$	$1.5 \times 10^{-10}(T/298)^{-0.27}\exp(38.5/T)$	Add reaction	NIST
$NH + CH_4 \rightarrow NH_2 + CH_3$	$1.49 \times 10^{-10}\exp(-10,103/T)$	Add reaction	NIST
$NH + C_2H_6 \rightarrow NH_2 + C_2H_5$	$1.16 \times 10^{-10}\exp(-8420.3/T)$	Add reaction	NIST
$NH + OH \rightarrow NH_2 + O$	$2.94 \times 10^{-12}(T/298)^{0.1}\exp(-5800/T)$	Revise rate	NIST
$NH_2 + CH_4 \rightarrow NH_3 + CH_3$	$5.75 \times 10^{-11}\exp(-6952/T)$	Revise rate	NIST
$H + H \xrightarrow{M} H_2$	$k_0 = \min(8.85 \times 10^{-33}(T/298)^{-0.6}, 1.0 \times 10^{-32})$	Revise k_0;	NIST
	$k_\infty = 1.0 \times 10^{-11}$	Add k_∞	Moses et al. (2005)
$H + CH_3 \xrightarrow{M} CH_4$	$k_0 = 6.0 \times 10^{-29}\max(T/298, 1.0)^{-1.8}$	Revise k_0 at $T \leqslant 298$ K;	NIST;
	$k_\infty = 1.92 \times 10^{-8}(\max(T, 110)^{-0.5}\exp(-400/\max(T, 110))$	Add k_∞	Moses et al. (2005)
	$F_c = 0.3\ +\ 0.58\exp(-T/800)$		
$H + C_2H \xrightarrow{M} C_2H_2$	$k_0 = 1.26 \times 10^{-18}T^{-3.1}\exp(-721/T)$	Add k_0	Moses et al. (2005)
	$k_\infty = 3.0 \times 10^{-10}$		
$H + C_2H_2 \xrightarrow{M} C_2H_3$	$k_0 = 3.31 \times 10^{-30}\exp(-740/T)$	Add k_∞	NIST
	$k_\infty = 1.4 \times 10^{-11}\exp(-1300/T)$		
	$F_c = 0.44$		
$H + C_2H_3 \xrightarrow{M} C_2H_4$	$k_0 = 2.3 \times 10^{-24}T^{-1}$	Add k_0;	Moses et al. (2005)
	$k_\infty = 1.8 \times 10^{-10}$	Revise k_∞	
$H + C_2H_4 \xrightarrow{M} C_2H_5$	$k_0 = \max(1.3 \times 10^{-29}\exp(-380/T), 3.7 \times 10^{-30})$	Revise k_0 at $T \leqslant 300$ K;	NIST;
	$k_\infty = 6.6 \times 10^{-15}T^{1.28}\exp(-650/T)$	Add k_∞	Moses et al. (2005)
	$F_c = 0.24\exp(-T/40) + 0.76\exp(-T/1025)$		
$H + C_2H_5 \xrightarrow{M} C_2H_6$	$k_0 = 4.0 \times 10^{-19}T^{-3}\exp(-600/T)\ (T > 200\ K)$	Revise k_0;	Moses et al. (2005)
	$k_0 = 2.49 \times 10^{-27}\ (T \leqslant 200\ K)$		
	$k_\infty = 2.0 \times 10^{-10}$		
$C + H_2 \xrightarrow{M} CH_2$	$k_0 = 6.89 \times 10^{-32}$	Add k_∞	NIST
	$k_\infty = 2.06 \times 10^{-11}\exp(-57/T)$		
$CH + H_2 \xrightarrow{M} CH_3$	$k_0 = 9.0 \times 10^{-31}\exp(550/T)$	Revise k_0 and k_∞	NIST
	$k_\infty = 2.01 \times 10^{-10}(T/298)^{0.15}$		Moses et al. (2005)
$CH_3 + CH_3 \xrightarrow{M} C_2H_6$	$k_0 = 1.68 \times 10^{-24}(T/298)^{-7}\exp(-1390/T)\ (T > 300\ K)$	Revise k_0 at $T \leqslant 300$ K;	NIST;
	$k_0 = 6.15 \times 10^{-18}T^{-3.5}\ (T \leqslant 300\ K)$	Add k_∞	Moses et al. (2005)
	$k_\infty = 1.12 \times 10^{-9}T^{-0.5}\exp(-25/T)$		
	$F_c = 0.62\exp(-T/1180) + 0.38\exp(-T/73)$		

Note. The rate constants of two-body reactions and the high-pressure limiting rate constants of three-body reactions (k_∞) have a unit of cm^3 molecule^{-1} s^{-1}, and the low-pressure limiting rate constants of three-body reactions (k_0) have a unit of cm^6 molecule^{-2} s^{-1}. The rates of three-body reactions are $k_0 k_\infty [M]/(k_\infty + k_0[M])F_c^\beta$, where $[M]$ is the number density of the atmosphere, and $\beta = (1 + (\log_{10}(k_0[M]/k_\infty))^2)^{-1}$. $F_c = 0.6$ unless otherwise noted. NIST = NIST Chemical Kinetics Database (http://kinetics.nist.gov).

Jupiter and the actual flux can conceivably be different. The impact of this additional H is limited to the upper atmosphere and, in most of our cases, is swamped by the H from the photodissociation of H_2O (see Section 3.4).

Since the modeled domain of the atmosphere includes the stratosphere and a small section of the upper troposphere, the standard mixing-length scaling (Gierasch & Conrath 1985) is not applicable to estimate the eddy diffusion coefficient. We instead anchor our choice of the eddy diffusion coefficient on

the value in the upper troposphere of Jupiter ($\sim 1 \times 10^3$ cm^2 s^{-1}, Conrath & Gierasch 1984) and explore a larger value in the study. Above the tropopause, we assume that mixing is predominantly caused by the breaking of gravity waves and the eddy diffusion coefficient is inversely proportional to the square root of the number density (Lindzen 1981).

Because the pressure range of the photochemical model typically includes the condensation of NH_3 and H_2O, we have added a scheme to account for the condensation of NH_3 into the
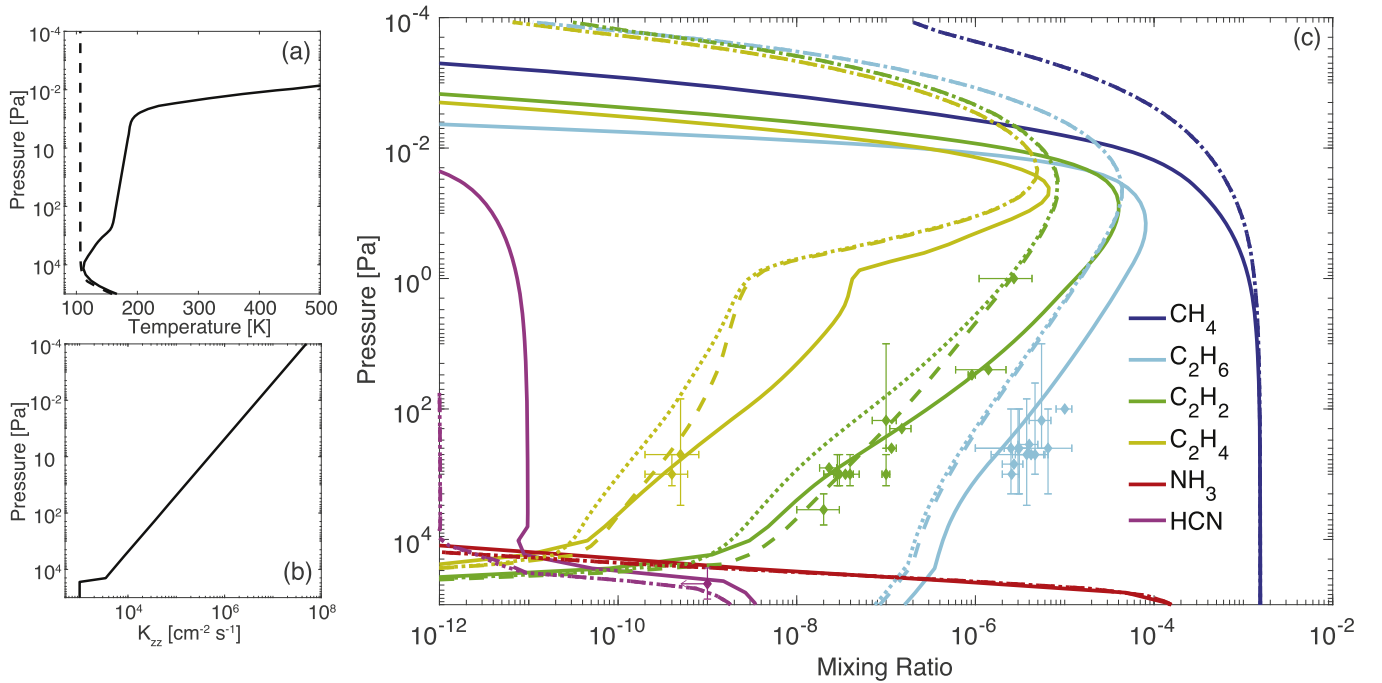
Figure 1. Jupiter as a test case. The planet modeled is a Jupiter-mass and Jupiter-radius planet at a 5.2 au orbit of a Sun-like star, having an atmospheric metallicity of $3 \times$ solar. (a) The solid line is the pressure–temperature profile adopted from Galileo probe measurements and Cassini CIRS measurements in Jupiter (Seiff et al. 1998; Simon-Miller et al. 2006) and the dashed line is the pressure–temperature profile calculated by the atmospheric structure model. (b) The eddy diffusion coefficient profile adopted in this work. (c) The calculated mixing ratio profiles of CH_4, NH_3, and major photochemical products. The solid lines are the results using the measured temperature profile, the dashed lines are the results using the modeled temperature profile (i.e., without the temperature inversion), and the dotted lines are the results using the modeled temperature profile and the photodissociation quantum yield of C_2H_2 set to unity (see discussion in Section 2.3). In comparison are the abundance data of major hydrocarbons and HCN in Jupiter's atmosphere, as compiled in Morrissey et al. (1995), Gladstone et al. (1996), Davis et al. (1997), Yelle et al. (2001), and Moses et al. (2005).

photochemical model, with that for H_2O already included in the model of Hu et al. (2012). In addition, we have added the schemes of condensation for N_2H_4 and HCN, the two main photochemical gases expected to condense in Jupiter's upper troposphere (e.g., Atreya et al. 1977; Moses et al. 2010). The low-temperature vapor pressures of N_2H_4 and HCN are adopted from Atreya et al. (1977) and Krasnopolsky (2009), respectively. As such, these gases are treated in the photochemical model and their production and removal paths including chemical reactions and condensation are self-consistently computed. This is important because, for example, NH_3 above the clouds in Jupiter is expected to be completely removed by photodissociation and converted to N_2H_4 and N_2, followed by condensation and transport to the deep atmosphere (Strobel 1973; Atreya et al. 1977; Kaye & Strobel 1983a, 1983b; Moses et al. 2010). As we will show in Section 3, the condensation of N_2H_4 and HCN limits their abundance in the middle atmosphere of cold planets like Kepler-167 e. For H_2S, we make a binary choice: if the cloud model indicates NH_4SH formation, we remove sulfur chemistry from the model, because NH_4SH should completely sequester H_2S (Atreya & Romani 1985); and we include the sulfur chemistry if NH_4SH cloud is not formed. This simplifies the calculations of sulfur photochemistry and is broadly valid when N/S > 1 in the bulk atmosphere.

We calculate the cross sections and single scattering albedo of ammonia and water cloud particles using their optical properties (Palmer & Williams 1974; Martonchik et al. 1984) and the radiative properties of the sulfur haze particles in the same way as Hu et al. (2013). NH_4SH and HCN condensates are treated the same way as NH_3 clouds. N_2H_4 condensates

have a very low abundance in all models and do not contribute significantly to the opacity. Thus, our model includes the absorption and scattering of cloud and haze particles when calculating the radiation field that drives photochemical reactions in the atmosphere.

2.3. Jupiter as a Test Case

As a test case, we have applied the coupled cloud condensation and photochemical model to a Jupiter-like planet and compared the results with the measured gas abundance in Jupiter and previous models of Jupiter's stratospheric composition (Atreya et al. 1977; Kaye & Strobel 1983a, 1983b; Gladstone et al. 1996; Moses et al. 2005, 2010). Figure 1 shows the pressure–temperature profile, eddy diffusion coefficient, and the mixing ratios of CH_4, NH_3, and major photochemical gases of the test case. The atmospheric structure model adequately predicts the tropospheric temperature profile and the pressure level of the tropopause, but it cannot generate a temperature inversion in the middle atmosphere (Figure 1, panel (a)). We have run the photochemical model with the pressure–temperature profile measured in Jupiter and the modeled pressure–temperature profile (i.e., without the temperature inversion) to see how much the photochemical gas mixing ratios change.

We find that the photochemical model can predict the mixing ratios of C_2H_6, C_2H_2, and C_2H_4 measured in Jupiter's stratosphere, and the modeled profile of HCN is consistent with the upper limit in Jupiter's upper troposphere when the measured pressure–temperature profile is adopted (Figure 1, panel (c)). The only exception is the C_2H_2 mixing ratio at

~ 1 Pa, where the modeled mixing ratio is greater than the measured value by $2\sigma \sim 3\sigma$. This less-than-perfect performance may be due to the lack of C_3, C_4, and higher hydrocarbons in our reaction network. For example, Moses et al. (2005) was able to fit the C_2H_2 mixing ratio at ~ 1 Pa, together with other mixing ratio constraints, with a more complete hydrocarbon reaction network and specific choices in the eddy diffusion coefficient profiles for Jupiter's stratosphere. In terms of nitrogen photochemistry, our photochemical model finds that NH_3 is depleted by photodissociation to the cloud deck, and the vast majority of the net photochemical removal of NH_3 becomes N_2H_4 and then condenses out. A small fraction becomes N_2 and HCN. The abundance of HCN is low ($\sim 10^{-9}$) in the troposphere due to the photolysis of NH_3 and CH_4 occurring at well separated pressure levels, and is limited by the cold trap near the tropopause (Figure 1). These behaviors are qualitatively similar to the past models of Jupiter's nitrogen photochemistry (Atreya et al. 1977; Kaye & Strobel 1983a, 1983b; Moses et al. 2010).

Figure 1 also indicates that adopting the modeled pressure–temperature profile that does not have a stratosphere, while preserving the overall behavior of the atmospheric photochemistry, would underpredict the mixing ratios of C_2H_6 and C_2H_2 by approximately half an order of magnitude. We use the atmospheric structure model in this study for speedy exploration of the main photochemical behavior, and one should keep this context in mind when interpreting the results shown in Section 3.

Another interesting point to make is that the quantum yield of H in the photodissociation C_2H_2 has been convincingly measured to be 100% by recent experiments (Läuter et al. 2002). When producing the models shown as the solid and dashed lines in Figure 1, panel c, we have applied a quantum yield of 16% so that the top-of-atmosphere rate of $C_2H_2 + h\nu \rightarrow C_2H + H$ would match with the models of Gladstone et al. (1996) and Moses et al. (2005). Revising the quantum yield to 100%, as shown by the dotted lines in Figure 1, panel c, slightly reduces the steady-state mixing ratio of C_2H_6 and reduces the mixing ratio of C_2H_2 and C_2H_4 by a factor of ~ 5 in the lower stratosphere ($\sim 10^3$ Pa). The photodissociation of C_2H_2 is the main source of H in the lower stratosphere (e.g., Gladstone et al. 1996) and thus its quantum yield is important for the hydrocarbon chemistry in the lower stratosphere. However, a quantum yield of 100% would result in poor fits to the measured mixing ratios of C_2H_2 and C_2H_4, and this potential discrepancy suggests that additional consideration of the atmospheric photochemistry of Jupiter might be warranted. We adopt the quantum yield of 100% in the subsequent models.

2.4. Planet Scenarios

We use the temperate sub-Neptune K2-18 b as a representative case of temperate and gas-rich planets around M dwarf stars, and use the gas giants PH2 b and Kepler-167 e as the representative cases of temperate and cold planets around G and K stars (Table 2). The results for K2-18 b are generally applicable to temperate (mini-)Neptunes of M dwarf stars such as the recently detected TOI-1231 b. For K2-18 b, the interior structures, thermochemical abundances, and atmospheric circulation patterns have been studied (Benneke et al. 2019; Madhusudhan et al. 2020; Piette & Madhusudhan 2020; Blain et al. 2021; Charnay et al. 2021), but the effects of atmospheric
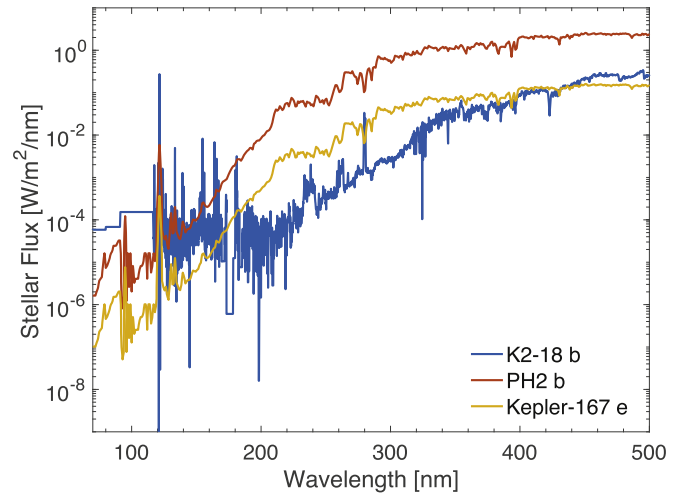

Figure 2. Incident stellar flux at the top of the atmospheres adopted in this study.

Table 2
Planetary Parameters Adopted in this Study

Planet	K2-18 b	PH2 b	Kepler-167 e
M_p ($M_\oplus$)	8.63[a]	N/A	N/A
R_p ($R_\oplus$)	2.61[b]	9.40[c]	9.96[c]
Insolation (Earth)	1.0[a]	1.2[d]	0.075[e]
Stellar Type	M	G	K

Notes.
[a] Benneke et al. (2019).
[b] Cloutier et al. (2019).
[c] Berger et al. (2018).
[d] Wang et al. (2013).
[e] Kipping et al. (2016).

photochemistry remain to be studied. Kepler-167 e is considered a "cold" exoplanet because it only receives stellar irradiation 7.5% of Earth's. The equilibrium cloud condensation model would predict NH_3 to condense in its atmosphere and form the uppermost cloud deck, below which NH_4SH solids form and scavenge sulfur from the above-cloud atmosphere. In the atmospheres of K2-18 b and PH2 b, only H_2O is expected to condense and forms the cloud deck—and thus the physical distinction between "temperate" and "cold."

The UV spectrum of K2-18 has not been measured and so we adopt that of GJ 176, a similar M dwarf star with the UV spectrum measured in the MUSCLES survey (France et al. 2016). The reconstructed Lyα flux of GJ 176 is similar to the measured flux of K2-18 (dos Santos et al. 2020). We adopt the UV spectrum of the Sun for the models of PH2 b and Kepler-167 e, even though Kepler-167 is a K star. Figure 2 shows the incident stellar flux at the top of the atmospheres adopted in this study. K2-18 b, while having a similar total irradiation to that of PH2 b, receives considerably less irradiation in the near-ultraviolet.

For these planets, we simulate H_2-dominated atmospheres having 1–100×solar metallicities. The higher-than-solar metallicity scenario may be particularly interesting for sub-Neptunes like K2-18 b because of a proposed mass–metallicity relationship that posits a less massive planet should have a higher metallicity (Thorngren et al. 2016). For PH2 b and Kepler-167
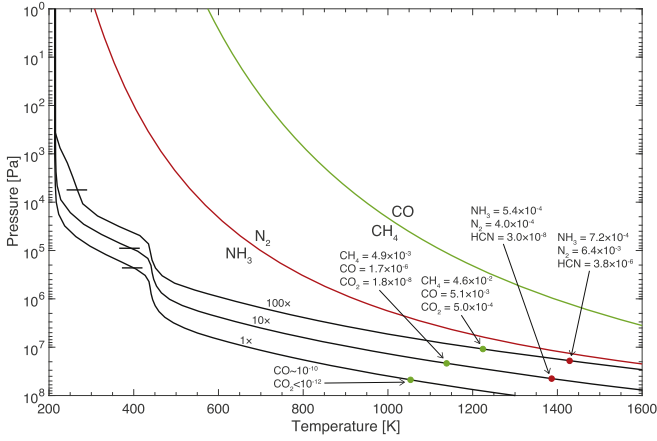
Figure 3. Pressure–temperature profiles of the temperate sub-Neptune K2-18 b for varied atmospheric metallicities and an internal heat flux of $T_{int} = 60$ K (similar to Neptune). The short horizontal bars show the lower boundary of the photochemical model (i.e., the pressure level 10-fold greater than the tropopause pressure). The green and red lines show the equal-abundance boundaries for major carbon and nitrogen gases in a solar metallicity gas in thermochemical equilibrium, and the green and red dots show the expected quench point for CO and that for N_2 respectively. The equilibrium mixing ratios of major C and N molecules at the respective quench points are shown.

Figure 4. The same as Figure 3 but for the planetary parameters of PH2 b and an internal heat flux of $T_{int} = 100$ K (similar to Jupiter).

Figure 5. The same as Figure 3 but for the planetary parameters of Kepler-167 e and an internal heat flux of $T_{int} = 100$ K (similar to Jupiter).

e, we assume as fiducial values a surface gravity of $25\,\mathrm{m\,s^{-2}}$ and an internal heat flux that corresponds to $T_{int} = 100$ K, similar to the parameters of Jupiter. Changing the surface gravity to $100\,\mathrm{m\,s^{-2}}$ results in slightly different cloud pressures and above-cloud abundances of gases on these planets, but does not change the qualitative behaviors of the atmospheric chemistry. For K2-18 b we assume an internal heat flux that corresponds to $T_{int} = 60$ K, similar to that of Neptune.

In the standard models, we assume that the dominant O, C, N, and S species are H_2O, CH_4, NH_3, and H_2S at the base of the photochemical domain. Gases and aerosols produced in the photochemical domain can be transported through the lower boundary, and thus the standard model setup implicitly assumes that thermochemical recycling in the deep troposphere effectively recycles the photochemical products into H_2O, CH_4, NH_3, and H_2S. Here, we quantitatively assess how realistic this assumption is based on the quench-point theory (e.g., Visscher & Moses 2011; Moses et al. 2013; Hu & Seager 2014; Zahnle & Marley 2014; Tsai et al. 2018). In that theory, the "quench point" is defined as the pressure level where the chemical lifetime of a gas equals the vertical mixing timescale (typically at the pressure of 10^7 Pa or higher). The gas is close to thermochemical equilibrium at the quench point, and its mixing ratio is carried to the atmosphere above the quench point by vertical mixing.

Figures 3–5 show the pressure–temperature profiles of the three planets calculated by the atmospheric structure model, and the mixing ratios of major C and N molecules at the respective quench points. We adopt the chemical lifetime of the CO$\longleftrightarrow$CH$_4$ and N$_2\longleftrightarrow$NH$_3$ conversions from Zahnle & Marley (2014) and estimate the eddy diffusion coefficient in the deep troposphere using the mixing-length theory in Visscher et al. (2010). The eddy diffusion coefficient depends on the assumed internal heat flux and has a typical value of $\sim 10^4\,\mathrm{m^2\,s^{-1}}$ at the pressure of 10^6–10^8 Pa. The quench point of CO_2 follows that of CO, and, similarly, that of HCN occurs at a similar pressure and temperature as N_2 (Zahnle & Marley 2014; Tsai et al. 2018). The mixing ratios of gases at the quench points are
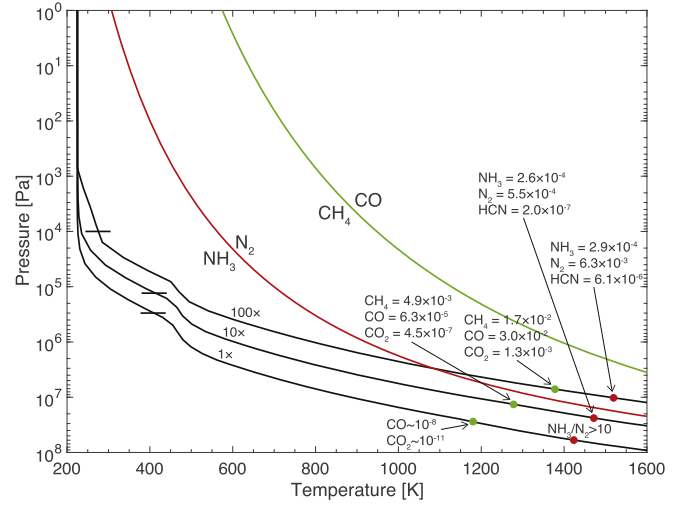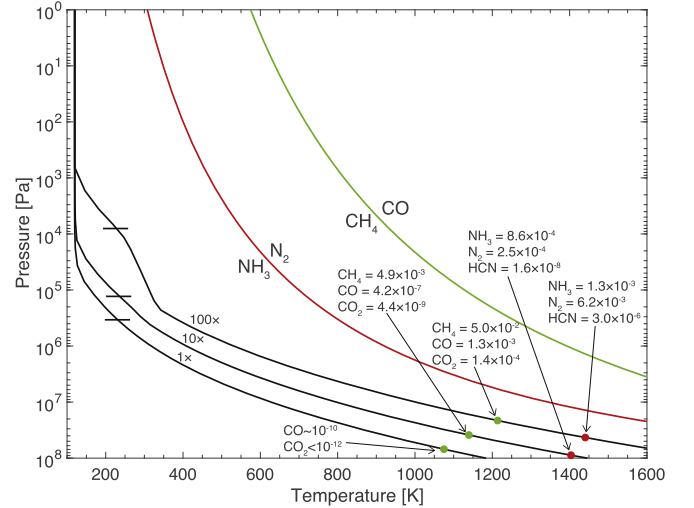
calculated using the thermochemical equilibrium model of Hu & Seager (2014).

Figures 3–5 show that a solar metallicity atmosphere is likely deep in the CH_4- and NH_3-dominated regime at the quench points on all three planets. Specifically, we find the mixing ratio of CO $\leqslant 10^{-8}$, that of $CO_2 \leqslant 10^{-11}$, and the mixing ratio of NH_3 greater than that of N_2 by >10-fold. With $10 \times$ solar metallicity, the atmosphere remains CH_4 dominated, but the mixing ratio of CO transported from the deep troposphere can be on the order of $10^{-6} \sim 10^{-5}$ and thus non-negligible. With the assumed internal heat flux and the modeled strength of deep-tropospheric mixing, the mixing ratio of N_2 can be comparable to that of NH_3 at the quench point. As N_2 does not have strong spectral features and is not a feedstock molecule for photochemistry, the effect of a hot interior would be mostly seen as a reduction of the mixing ratio of NH_3. The impact of the hot interior is the most significant in the $100 \times$ solar metallicity atmosphere. Both CO and CO_2 have mixing ratios >10^{-4} at the quench point, and in the hottest case (PH2 b), the mixing ratio CO is greater than that of CH_4. For nitrogen, the

mixing ratio of NH_3 can be reduced by a factor of $10 \sim 100$ at the thermochemical equilibrium in the deep troposphere.

As a general trend, a higher deep-atmosphere temperature favors CO, CO_2, and N_2, and reduces the equilibrium abundance of NH_3. We have thus run variant models for the $10 \times$ and $100 \times$ solar metallicity cases, and used the mixing ratios of CH_4, CO, CO_2, NH_3, and N_2 at the quench points as shown in Figures 3–5 as the lower boundary conditions. Technically the mixing ratio of deep H_2O is also affected, but the photochemical models have lower boundaries that are well above the base of the water cloud, and are thus immune to small changes in the input water abundance. Also, we do not fix the lower boundary mixing ratio of HCN in these models, because the mixing ratio of HCN at the quench point does not exceed the mixing ratio found by the photochemical models at the lower boundary in any case. We emphasize that specific quantities of the input gas abundance depend on the detailed thermal structure of the interior, which is related to the thermal history of the planet and exogenous factors like tidal heating, as well as the strength of vertical mixing in the interior (Fortney et al. 2020). For example, applying an internal heat flux that corresponds to $T_{int} = 30$ K (similar to Earth) largely restores the CH_4 and NH_3 dominance for the three planets. While these factors are likely uncertain for many planets to be observed, the standard and variant photochemical models presented in this paper give an account of the range of possible behaviors that manifest in the observable part of the atmosphere.

3. Results

3.1. Main Behaviors of Atmospheric Chemistry

The abundance profiles of the equilibrium gases (H_2O, CH_4, NH_3, and H_2S) and their main photochemical products are shown in Figures 6–8. In all models, we find that the main photochemical products are C_2H_6, C_2H_2, CO, CO_2, N_2, HCN, N_2O, and elemental sulfur haze, but the abundance of these species and their pressure dependency differ significantly from model to model.

3.1.1. K2-18 b: a Temperate Planet around an M Star

For K2-18 b, our model predicts that water condenses to form a cloud at the pressure of $\geqslant 10^4$ Pa for the solar and $10 \times$ solar cases, and at the pressure of $\sim 10^3$ Pa for the $100 \times$ solar case. Above the cloud, the mixing ratio of water is depleted by approximately one order of magnitude, but not totally depleted. The pressure of cloud for the $100 \times$ solar abundance case we model is consistent with predictions of a non-gray radiative-equilibrium model and a 3D climate model, but those models do not predict a water cloud for the solar and $10 \times$ solar abundance (Blain et al. 2021; Charnay et al. 2021). Given the small degree of water depletion found in our models, this discrepancy does not lead to substantial errors in the results of the above-cloud photochemistry.

Both CH_4 and H_2O are photodissociated at the pressure of approximately 0.1–1 Pa. The photodissociation results in the formation of C_2H_6, C_2H_2, CO, and CO_2. C_2H_2 has a high mixing ratio at the pressure where the photodissociation takes place but is quickly depleted toward higher pressures. In the middle atmosphere (~ 10–10^3 Pa), CO, CO_2, and C_2H_6 can have a mixing ratio of ~ 1 parts-per-million (ppm) for the $100 \times$ solar abundance case, and the mixing ratio of these photochemical gases is <1 ppm for lower metallicities. When

the deep-tropospheric source of CO and CO_2 is applied to the bottom of the photochemical domain, the mixing ratio of CO at 10^2 Pa is ~ 1 ppm for the $10 \times$ solar cases, but it can reach ~ 4000 ppm for the $100 \times$ solar case. The mixing ratio of CO_2 at 10^2 Pa can reach ~ 500 ppm for the $100 \times$ solar case.

NH_3 is photodissociated at the pressure of $1 \sim 10$ Pa. The photodissociation results in the formation of N_2 and HCN with similar yields. The mixing ratio of HCN at $\sim 10^2$ Pa is ~ 6, 50, and 500 ppm for the solar, $10 \times$ solar, and $100 \times$ solar abundance cases, respectively. If the mixing ratio of NH_3 in the deep troposphere is applied to the bottom of the photochemical domain, the resulting mixing ratio of HCN does not change significantly in the $10 \times$ solar case but decreases to ~ 100 ppm in the $100 \times$ solar case.

Lastly, H_2S is photodissociated at approximately the same pressure as the water cloud. The photodissociation leads to the formation of elemental sulfur (S_8) haze, as predicted previously (Zahnle et al. 2016). The haze layer extends to an altitude only slightly higher than the water cloud deck.

3.1.2. PH2 b: a Temperate Planet around a G/K Star

PH2 b has a slightly higher insolation and temperature than K2-18 b, but it receives much more near-ultraviolet irradiation (Figure 2). The water condensation and small degree of depletion above the cloud, as well as the photodissociation of H_2S and the location of the sulfur haze layer, are similar to those predicted for K2-18 b.

CH_4 is photodissociated at the pressure of 0.1–1 Pa, and H_2O is photodissociated at 1–10 Pa. The main products of these photodissociations are still C_2H_6, C_2H_2, CO, and CO_2. Instead of CO in the case of K2-18 b, CO_2 is the most abundant photochemical gas in the middle atmosphere (~ 10–10^3 Pa), and its mixing ratio is 2–10 ppm, 5–40 ppm, and 40–200 ppm for the solar, $10 \times$ solar, and $100 \times$ solar abundance cases, respectively. The mixing ratio of CO is less by approximately one order of magnitude, and that of C_2H_6 is ~ 1 ppm for the $100 \times$ solar case and <1 ppm for lower metallicities.

As a striking difference from the M star case (K2-18 b), NH_3 is fully depleted by photodissociation above the water cloud deck. The mixing ratio of NH_3 in the middle atmosphere is minimal. The photodissociation also leads to the formation of N_2 and HCN, with HCN being the most abundant photochemical product. The mixing ratio of HCN in the middle atmosphere reaches ~ 100, 700, and 10,000 ppm for the solar, $10 \times$ solar, and $100 \times$ solar abundance cases, respectively.

With a Jupiter-like internal heat flux, the equilibrium chemistry in the deep troposphere may substantially change the chemical composition in the photochemical domain. In the $10 \times$ solar cases, the mixing ratio of CO in the middle atmosphere can reach ~ 10 ppm and that of CO_2 ~ 60 ppm. HCN would no longer be the most abundant nitrogen product, and its mixing ratio in the middle atmosphere can be reduced to ~ 40 ppm. In the $100 \times$ solar cases, both CO and CO_2 can have very high mixing ratios ($>10^{-2}$, and on the same order of CH_4) in the middle atmosphere, and the above-cloud H_2O would be consumed by photochemistry and have a mixing ratio of ~ 10 ppm at 10^2 Pa. The mixing ratio of HCN would be further reduced to ~ 10 ppm, while still marginally greater than the mixing ratio at the quench point.
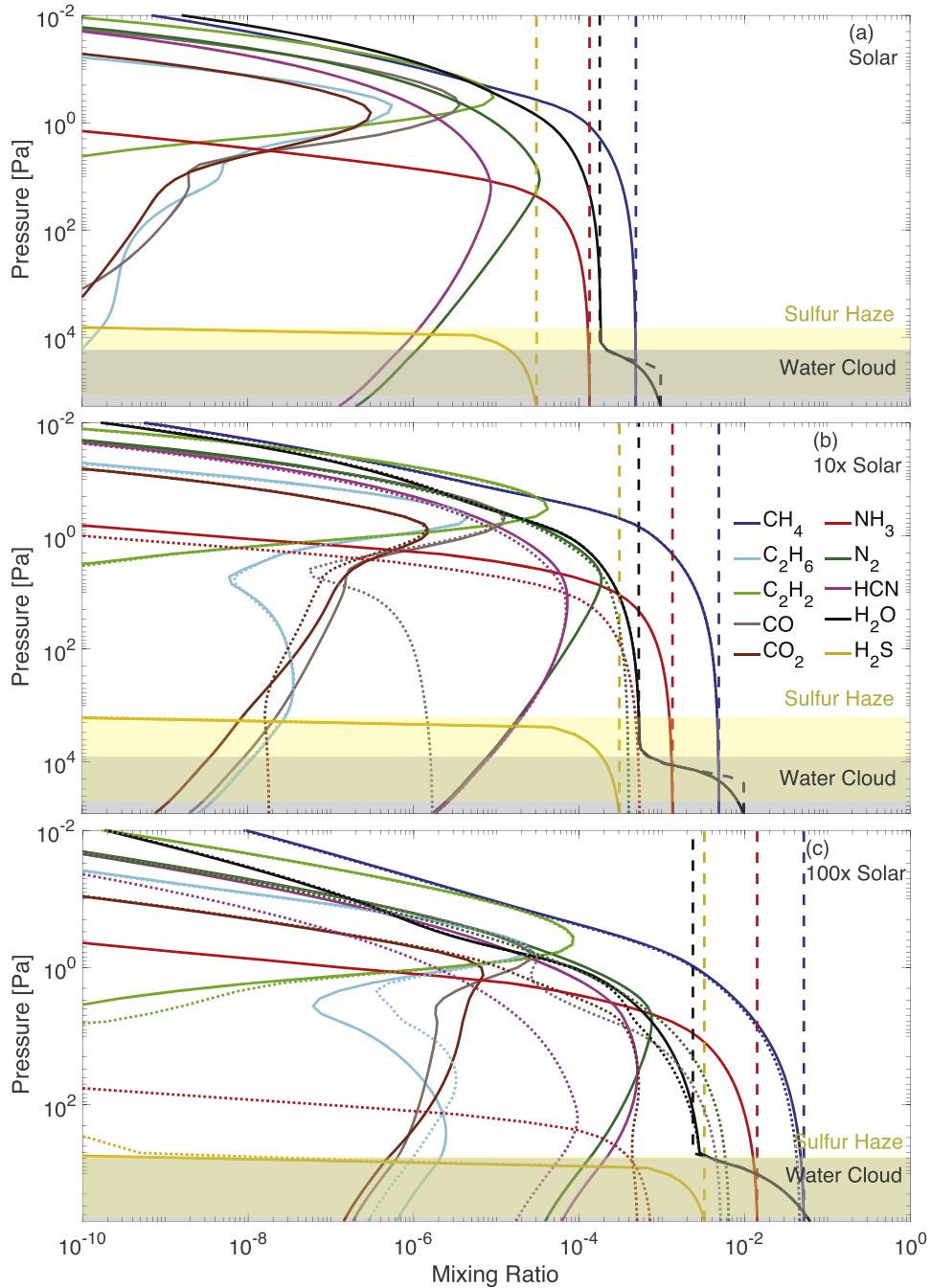
Figure 6. Modeled abundances of main gases and photochemical products in the temperate sub-Neptune K2-18 b for varied metallicities. Solid lines show the photochemical model results and the dashed lines show the equilibrium cloud condensation model results for comparison. Dotted lines in panels (b) and (c) show the photochemical model results that adopt the quench-point abundances of CH_4, CO, CO_2, NH_3, and N_2 (Figure 3) at the lower boundary.

3.1.3. Kepler-167 e: a Cold Planet around a G/K Star

The atmosphere of Kepler-167 e is much colder than that of K2-18 b or PH2 b, and its atmospheric chemistry is more akin to that of Jupiter (Atreya et al. 1977; Kaye & Strobel 1983a, 1983b; Gladstone et al. 1996; Moses et al. 2005, 2010). Both H_2O and H_2S are fully depleted by condensation or NH_4SH formation, and the uppermost cloud predicted by the atmospheric structure model is NH_3 ice. However, the steady-state results of the photochemical model indicate that photodissociation of NH_3 should deplete the NH_3 ice cloud. NH_3 is photochemically depleted to the pressure of 7×10^4–10^3 Pa from the solar to $100 \times$ solar abundance cases. The

main product of the photodissociation that can accumulate in the middle atmosphere is N_2, while the mixing ratios of HCN and N_2H_4 are limited by condensation. The mixing ratio of HCN can reach >1 ppm below the condensation level in the $100 \times$ solar case.

The main photochemical gases of carbon are C_2H_6 and C_2H_2, with no CO or CO_2 at appreciable mixing ratios. While the mixing ratio of C_2H_2 strongly peaks at 0.1 Pa, where the photodissociation of CH_4 takes place, the mixing ratio of C_2H_6 can be significant in the middle atmosphere. At 10^2 Pa, the mixing ratio of C_2H_6 is $\sim$2, 4, and 30 ppm for the solar, $10 \times$ solar, and $100 \times$ solar abundance cases, respectively. If
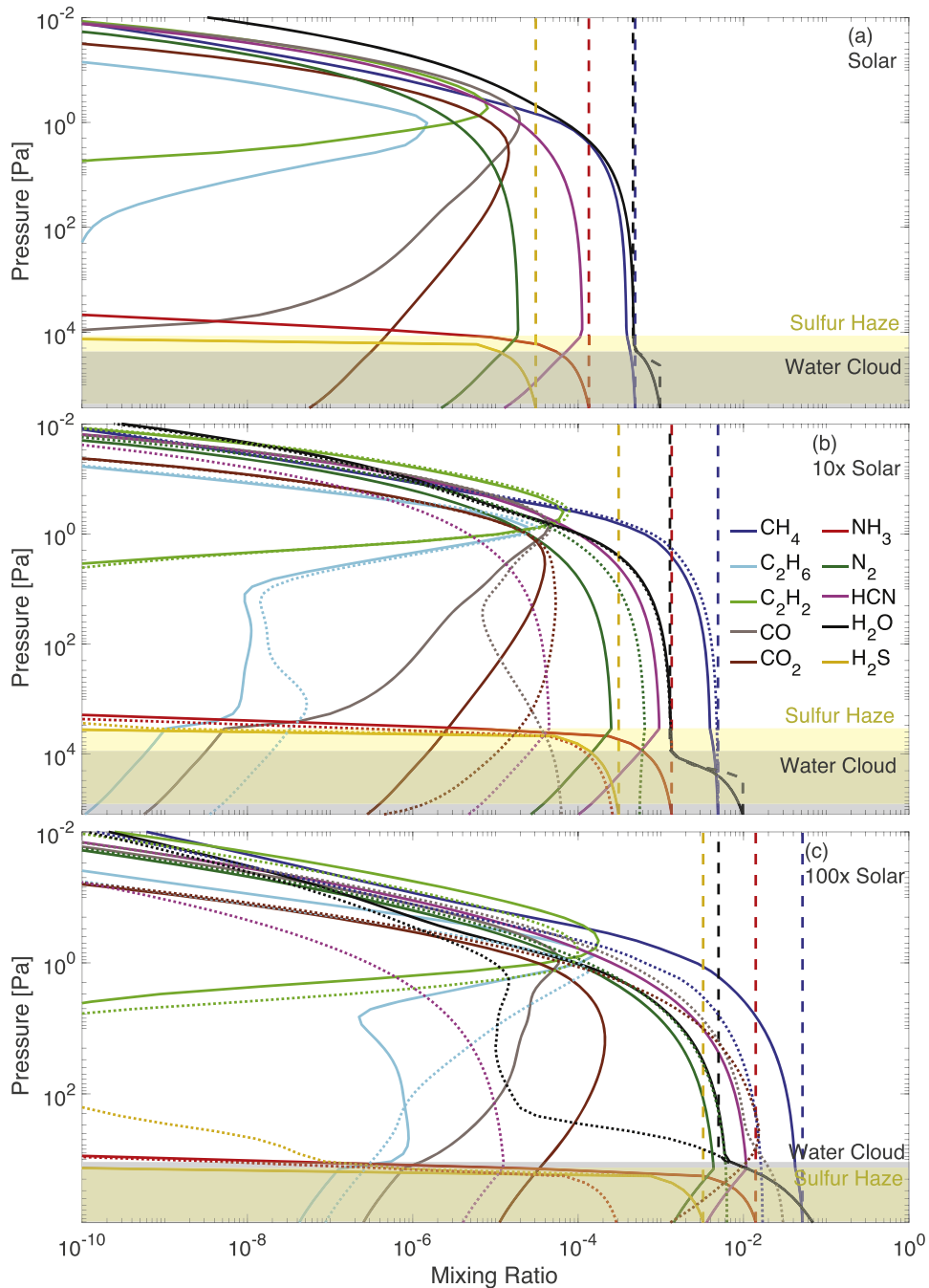
Figure 7. Modeled abundances of main gases and photochemical products in the temperate gas giant PH2 b for varied metallicities. Solid lines show the photochemical model results and the dashed lines show the equilibrium cloud condensation model results for comparison. Dotted lines in panels (b) and (c) show the photochemical model results that adopt the quench-point abundances of CH_4, CO, CO_2, NH_3, and N_2 (Figure 4) at the lower boundary.

the deep-tropospheric source of CO and CO_2 is applied to the bottom of the photochemical domain, they can have substantial mixing ratios in the $100 \times$ solar case, while the mixing ratio of C_2H_6 is not strongly impacted.

3.2. Photochemical Depletion of NH_3

From Figures 6–8, we see that NH_3 is depleted to the cloud deck in temperate and cold planets around G/K stars but remains intact in the middle atmosphere of temperate and cold planets around M stars. This finding is significant because it

implies that NH_3 should be detectable on temperate planets around M stars but not around G/K stars (see Section 3.5).

The root cause of this different behavior is the M stars (represented by GJ 176 here) emit substantially lower irradiation at the near-ultraviolet wavelengths than do the G/K stars (represented by the Sun here; Figure 2). The radiation that dissociates NH_3 in the H_2-dominated atmosphere is the radiation that is not absorbed by the typically more abundant CH_4 and H_2O. NH_3 has a dissociation limit at $\sim$230 nm, while for CH_4 it is at $\sim$150 nm and for H_2O $\sim$240 nm, but the cross section and the shielding effect of H_2O is small, $>$200 nm (Hu et al. 2012; Ranjan et al. 2020). C_2H_2 also absorbs photons up
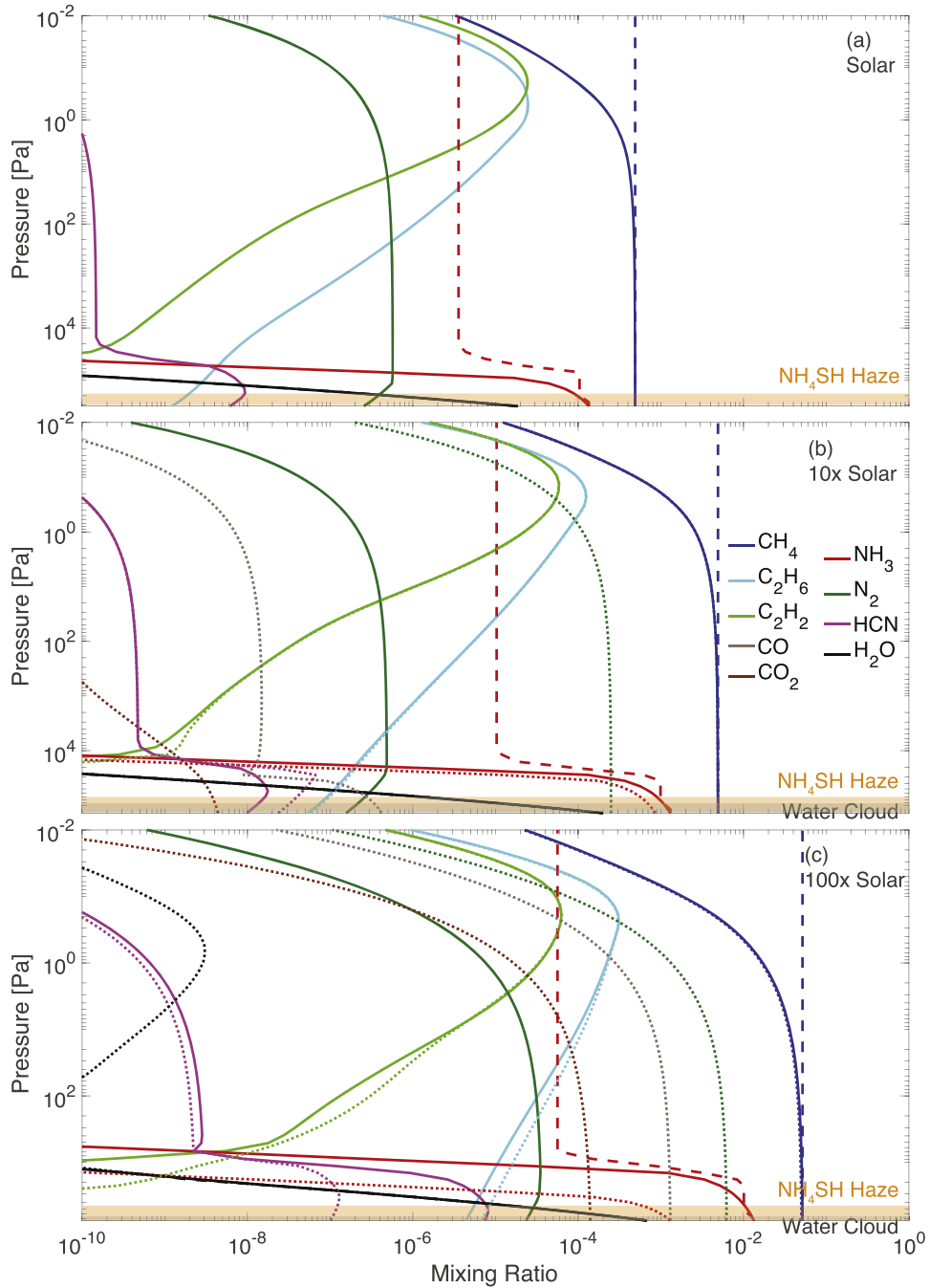
Figure 8. Modeled abundances of main gases and photochemical products in the cold gas giant Kepler-167 e for varied metallicities. Solid lines show the photochemical model results and the dashed lines show the equilibrium cloud condensation model results for comparison. Dotted lines in panels (b) and (c) show the photochemical model results that adopt the quench-point abundances of CH_4, CO, CO_2, NH_3, and N_2 (Figure 5) at the lower boundary.

to ∼230 nm but it typically does not strongly interfere with the NH_3 photodissociation due to its relatively low abundance. Thus, photons in the range 200–230 nm are the most relevant for the photodissociation of NH_3 in K2-18 b and PH2 b, and photons in the range 150–230 nm are the most relevant for Kepler-167 e. Having similar bolometric irradiation, the photon flux at 200–230 nm received by PH2 b is more than that received by K2-18 b by >2 orders of magnitude (Figure 2). The photon flux received by Kepler-167 e is one order of magnitude more than for K2-18 b, and the removal of NH_3 by condensation further pushes down the pressure of photochemical depletion (see below).

3.2.1. Criterion of Photochemical Depletion

How does the photon flux control the pressure of photochemical depletion? Guided by the numerical results, here we develop a simple theory that estimates the pressure of photochemical depletion. Assuming that photodissociation is the only process that removes NH_3 with no recycling or production, its mixing ratio profile at the steady state should obey the following differential equation:

$$\frac{d}{dz}\left(KN\frac{df}{dz}\right) = fNJ, \qquad (1)$$

where z is altitude, K is the eddy diffusion coefficient, N is the total number density of the atmosphere, f is the mixing ratio, and J is the photodissociation rate (often referred to as the "J-value" in the atmospheric chemistry literature). The number density has a scale height of H, and the equation can be rewritten as

$$\frac{d^2f}{dz^2} - \frac{1}{H}\frac{df}{dz} - \frac{J}{K}f = 0. \quad (2)$$

Assuming J, H, and K to be constant with respect to z, the equation above has the analytical solution of

$$f = f_0 \exp\left(\frac{z}{2}\left(\frac{1}{H} - \sqrt{\frac{1}{H^2} + \frac{4J}{K}}\right)\right) \equiv f_0 \exp\left(-\frac{\alpha z}{H}\right), \quad (3)$$

where f_0 is the mixing ratio at the pressure of photochemical depletion ($z = 0$ for simplicity), and α is

$$\alpha = \frac{1}{2}\left(\sqrt{1 + \frac{4JH^2}{K}} - 1\right). \quad (4)$$

Therefore, when the product $4JH^2/K$ is small, $\alpha \to 0$ and the mixing ratio profile is close to a constant; and when $4JH^2/K$ is large, α can be $\gg 1$ and thus the mixing ratio drops off very quickly. This explains the vertical profiles of NH_3 seen in Figures 6–8.

Going back to Equation (1), which can be integrated from the pressure of photochemical depletion to the top of the atmosphere, we have

$$KN\frac{df}{dz}\Big|_{z=\infty} - KN\frac{df}{dz}\Big|_{z=0} = \int_0^\infty n(z)J(z)dz, \quad (5)$$

where $n \equiv fN$ is the number density of NH_3. Assuming that the photoabsorption of NH_3 itself is the sole source of opacity, J can be expressed as

$$J(z) = J_\infty \exp\left(-\sigma \int_z^\infty n(z')dz'\right), \quad (6)$$

where J_∞ is the top-of-atmosphere J-value and σ is the mean cross section of NH_3. The differential of Equation (6) is

$$\frac{dJ}{dz} = \sigma n J. \quad (7)$$

Combining Equations (5) and (7), and recognizing df/dz vanishes at $z = \infty$, we obtain

$$-KN\frac{df}{dz}\Big|_{z=0} = \frac{1}{\sigma}\int_0^\infty \frac{dJ}{dz}dz = \frac{J_\infty - J(z=0)}{\sigma}. \quad (8)$$

With $J(z=0) \sim 0$ (i.e., the J-value immediately below the pressure of photochemical depletion is minimal), and $J_\infty = \sigma I$, where I is the photon flux at the top of the atmosphere, we obtain

$$-KN\frac{df}{dz}\Big|_{z=0} = I. \quad (9)$$

Note that to derive Equation (9), no specific profiles for J or n (f) need to be assumed.

The physical meaning of Equation (9) is that the number of NH_3 molecules that diffuse through the pressure of photochemical depletion should be equal to the number of photons
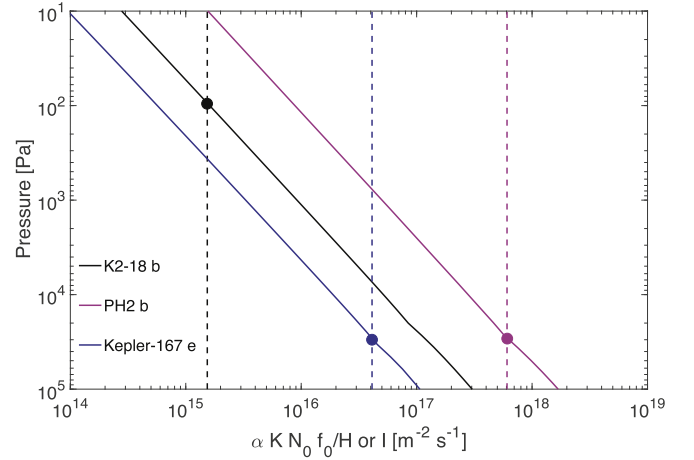

Figure 9. Pressure of photochemical depletion of NH_3 predicted by the criterion in Equations (9) and (10). We compare the left-hand side (solid line) and right-hand side (dashed line) of Equation (10), assuming a solar abundance atmosphere. Where the solid line and the dashed line meet defines the pressure of photochemical depletion.

received at the top of the atmosphere. This physical condition would become evident if one regards the column of NH_3 above the pressure of photochemical depletion as a whole and recognizes that one photon dissociates one molecule. To the extent that the photoabsorption of NH_3 itself is the dominant source of opacity, the criterion expressed by Equation (9) does not depend on the mean cross section. Similarly, the criterion will be applicable to any molecule subject to photodissociation in a wavelength range largely free of interference by other molecules.

It should be noted that Equation (9) cannot be derived by requiring the pressure of photochemical depletion to occur roughly at the optical depth of unity for the photodissociating radiation. This is because the mixing ratio profile in Equation (3) is valid only locally and depends on J, which in turns depends on the vertical profile of the mixing ratio. As such, one cannot integrate Equation (3) directly to find the pressure of photochemical depletion, and the optical-depth-of-unity condition is not as predictive as Equation (9).

The left-hand side of Equation (9) can be evaluated locally using Equation (3), and Equation (9) becomes

$$\frac{\alpha KN_0 f_0}{H} = I, \quad (10)$$

where N_0 and f_0 are the total number density and the mixing ratio at the pressure of photochemical depletion. The pressure is thus $P_0 = N_0 k_b T$ where k_b is the Boltzmann constant and T is temperature. The term α can be evaluated with Equation (4) for a J value that corresponds to 5% of the top-of-atmosphere value. Equation (10) thus provides a closed-form criterion that determines the pressure of photochemical depletion, and explains why the pressure of photochemical depletion is sensitive to the top-of-atmosphere flux of photons that drive photodissociation.

Figure 9 shows both sides of Equation (10) for the three planets modeled assuming a solar abundance atmosphere. We can see that the pressure of photochemical depletion implied by Equation (10) for K2-18 b is ~ 100 Pa, consistent with the pressure where the photochemical model starts to substantially deviate from the equilibrium cloud condensation model

(Figure 6). Figure 6 also shows that the mixing ratio NH_3 decreases very slowly near the pressure of the photochemical depletion, but the decrease becomes faster for lower pressures, where the J value and the $4JH^2/K$ product become greater (see Equations (3) and (4)). The mixing ratio of NH_3 eventually drops below 10^{-6} at the pressure lower than the pressure of photochemical depletion by approximately one order of magnitude. The pressures of photochemical depletion implied by Equation (10) for PH2 b and Kepler-167 e are close to or below the cloud deck (i.e., 10^4–10^5 Pa), which is consistent with numerical finding that NH_3 is photodissociated to the cloud deck on these planets (Figures 7 and 8). Therefore, although Equation (10) cannot replace the full photochemical calculation due to the underlying assumptions (e.g., no recycling or production, self-shielding only), it provides a guiding estimate of whether a gas is likely depleted by photodissociation in the middle atmosphere.

3.2.2. Sensitivity to the Eddy Diffusion Coefficient

From the criterion of photochemical depletion (Equation (10)), we see that when the eddy diffusion coefficient increases, the pressure of photochemical depletion decreases. In other words, stronger mixing would sustain a photodissociated gas (e.g., NH_3) to a lower pressure or higher altitude. We have used the photochemical model to conduct a sensitivity study of the eddy diffusion coefficient, and the results confirm this understanding (Figure 10). The most significant sensitivity happens with PH2 b: the standard model predicts the photodissociation would deplete NH_3 to the cloud deck, while with a 10-fold or 100-fold greater eddy diffusion coefficient, NH_3 would be depleted at $10^2 \sim 10^3$ Pa. For Kepler-167 e, with a 10-fold or 100-fold greater eddy diffusion coefficient, photodissociation can no longer deplete the NH_3 ice cloud, while the mixing ratio of NH_3 in the middle atmosphere remains small due to condensation and photodissociation above the cloud deck.

The top of the sulfur haze layer moves up in the atmosphere when the eddy diffusion coefficient increases. For both K2-18 b and PH2 b, the top of the sulfur haze would be at $\sim 10^3$ Pa and 10^2 Pa for 10-fold and 100-fold greater eddy diffusion coefficient (Figure 10). A haze layer that extends to 10^2 Pa would greatly interfere with transmission spectroscopy and also affect the spectra of the reflected starlight (see Section 3.5). This trend is consistent with the findings of Zahnle et al. (2016) and is produced by two effects acting together. First, the pressure of photochemical depletion of H_2S, the feedstock of sulfur haze, decreases for a greater eddy diffusion coefficient. Second, a stronger eddy diffusion helps increase the lifetime of haze particles against falling (see the formulation in Hu et al. 2012). For PH2 b, the extended sulfur haze layer further keeps NH_3 from photochemical depletion by absorbing the ultraviolet photons that can dissociate NH_3.

The sensitivity of main photochemical gases' abundance to the eddy diffusion coefficient is complex (Figure 10), which indicates several factors at work. For N_2 and HCN (the dominant photochemical gases of nitrogen), their mixing ratios at the lower boundary decrease with the eddy diffusion coefficient. This is because, in our model, gases move across the lower boundary at a velocity that is proportional to the eddy diffusion coefficient, and the loss to the lower boundary is the main loss mechanism for both N_2 and HCN. Their mixing ratios in the middle atmosphere do not necessarily follow the same trend, as they also depend on the photochemical production (see Section 3.3). The abundance of the photochemical gases of carbon does not depend on the eddy diffusion coefficient monotonically, and this is because the formation rates of CO, CO_2, and C_2H_6 largely depend on the abundance of H, OH, and O, which is in turn controlled by the full chemical network involving the photodissociation of CH_4, H_2O, and NH_3 (see Section 3.4). For example, in K2-18 b with the solar metallicity, both CO and CO_2 have very small mixing ratios in the middle atmosphere in the standard case; the two would be substantially more abundant in the middle atmosphere with a 10-fold greater eddy diffusion coefficient, and CO would become more abundant than CO_2 with a 100-fold greater eddy diffusion coefficient. These examples highlight the richness and complexity of atmospheric photochemistry in temperate and cold planets.

### 3.3. Photolysis of NH_3 in the Presence of CH_4

A common phenomenon that emerges from the photochemical models is the synthesis of HCN in temperate and H_2-rich exoplanets. The photodissociation of NH_3 in Jupiter leads to N_2 but not significant amounts of HCN, and this is mainly because NH_3 is dissociated at much higher pressures than CH_4 (e.g., Atreya et al. 1977; Kaye & Strobel 1983a, 1983b; Moses et al. 2010). HCN in Titan's N_2-dominated atmosphere mainly comes from the reactions between atomic nitrogen and hydrocarbons and the associated chemical network (Yung et al. 1984; Lavvas et al. 2008; Krasnopolsky 2014; Vuitton et al. 2019). Similar processes, as well as the reactions between CH and NO/N_2O may also lead to formation of HCN on early Earth or rocky exoplanets with N_2-dominated atmospheres irradiated by active stars (Airapetian et al. 2016; Rimmer & Rugheimer 2019). In addition, the formation of HCN has been commonly found in warm and hot H_2-rich exoplanets (e.g., Line et al. 2011; Moses et al. 2011; Venot et al. 2012; Agúndez et al. 2014; Mollière et al. 2015; Moses et al. 2016; Blumenthal et al. 2018; Kawashima & Ikoma 2018; Hobbs et al. 2019; Lavvas et al. 2019; Molaverdikhani et al. 2019), and the mechanisms identified include quench kinetics (Moses et al. 2011; Venot et al. 2012; Agúndez et al. 2014) and photochemistry (Line et al. 2011; Kawashima & Ikoma 2018; Hobbs et al. 2019). Here, we show that HCN can also build up to significant amounts in temperate exoplanets with H_2-dominated atmospheres.

Figure 11 shows the chemical network that starts with the photodissociation of NH_3 and ends with the formation of N_2 and HCN as the main photochemical products. The key condition for the synthesis of HCN is the photodissociation of NH_3 in the presence of CH_4 and at a temperature $> \sim 200$ K. This condition allows CH_3, one of the ingredients for the synthesis of HCN, to be produced locally by the reaction between CH_4 and H, and this H is produced by the photodissociation of NH_3 itself. We describe the details as follows.

The photodissociation of NH_3 mainly produces NH_2,

$$NH_3 \xrightarrow{h\nu} NH_2 + H, \qquad (R1)$$

and some of the NH_2 produced is returned to NH_3 via

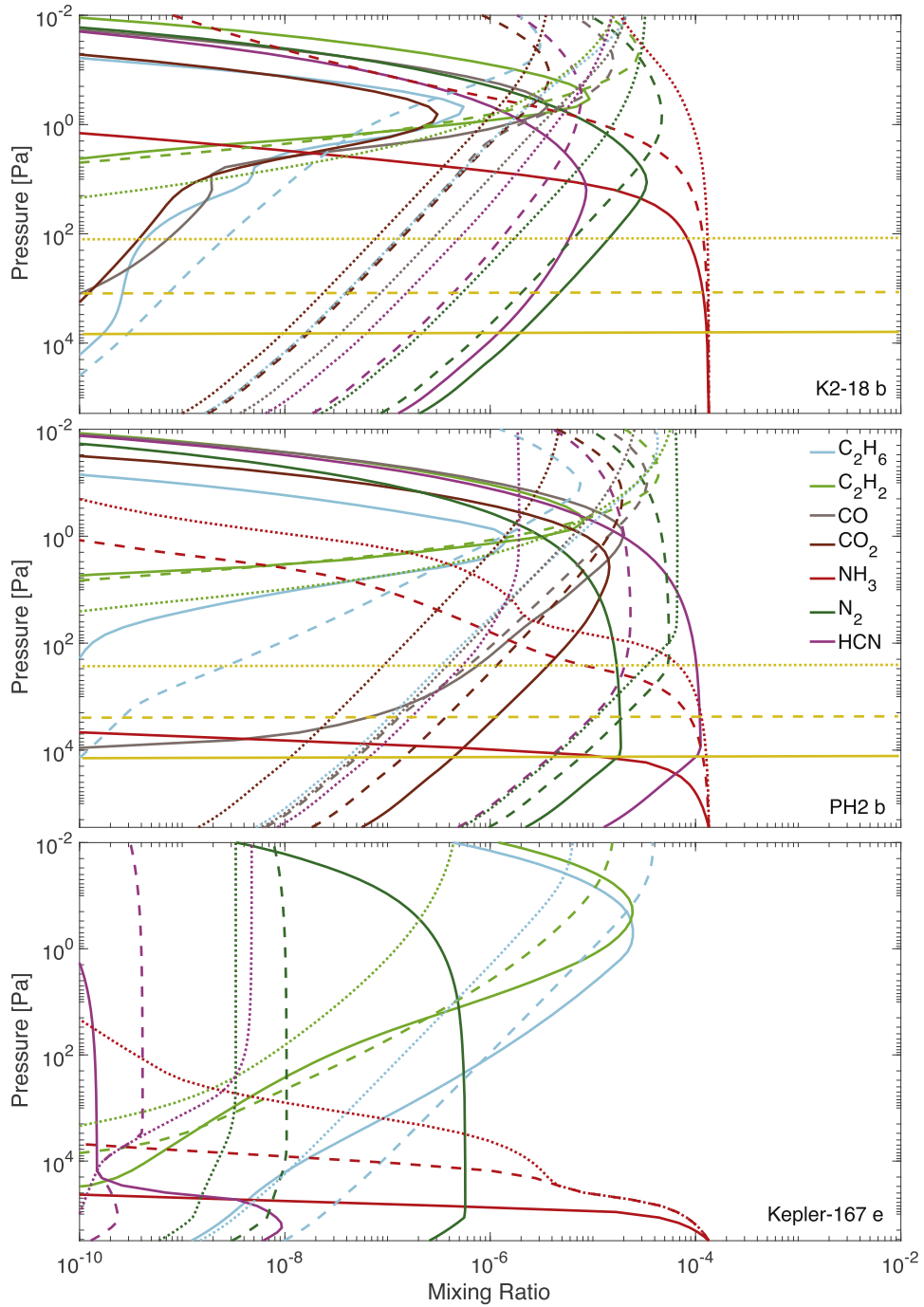$$NH_2 + H_2 \rightarrow NH_3 + H, \qquad (R2)$$
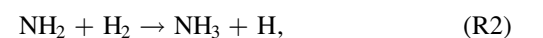
Figure 10. Sensitivity of the abundance profiles of NH_3 and main photochemical gases to the eddy diffusion coefficient. The profiles of H_2O and CH_4 are not shown because their abundance in the middle atmosphere is not sensitive to the eddy diffusion coefficient. The horizontal orange lines show the top of the sulfur haze layer. The solid lines show the standard model, and the dashed and dashed–dotted lines show the models with 10-fold and 100-fold greater eddy diffusion coefficients, respectively. These models assume the solar abundance. A greater eddy diffusion coefficient causes the photodissociation of NH_3 to occur at a lower pressure.

and

$$NH_2 + H \xrightarrow{M} NH_3. \qquad (R3)$$

Another channel of the photodissociation of NH_3 is to produce NH

$$NH_3 \xrightarrow{h\nu} NH + H_2. \qquad (R4)$$

The NH_2 channel requires photons more energetic than 230 nm and the NH channel requires photons more energetic than 165 nm. Therefore, the photons that produce NH are more easily shielded by H_2O and CH_4. For the three planets modeled, the NH channel is important in K2-18 b and Kepler-167 e, but not in PH2 b. This is because the photodissociation of NH_3 occurs at higher pressures in PH2 b and is subject to the shielding effect of both H_2O and CH_4. The NH channel mostly leads to N_2 (Figure 11).

The NH_2 that is not recombined to form NH_3 can undergo

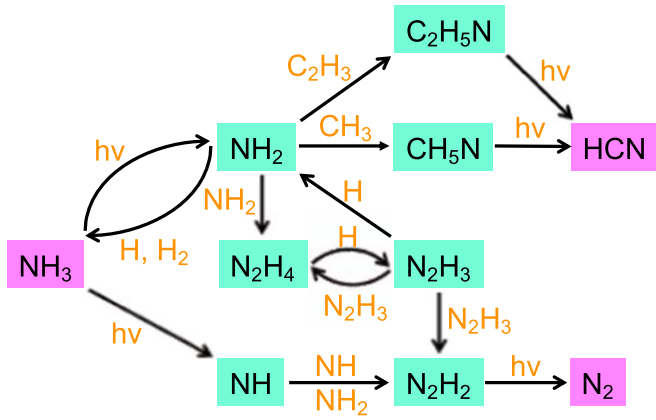$$NH_2 + NH_2 \rightarrow N_2H_4, \qquad (R5)$$

Figure 11. Chemical network from the photodissociation of NH_3 in temperate and H_2-dominated atmospheres. Not all reactions are shown, and the importance of the shown reactions changes from case to case. In the presence of CH_4, HCN is one of the main photochemical products.

and the N_2H_4 produced (if not condensed out) can then become N_2H_3. N_2H_3 can react with itself to form N_2H_2, whose photodissociation produces N_2, or with H to return to NH_2 (Figure 11). The other loss of NH_2 is to react with CH_3,

$$NH_2 + CH_3 \rightarrow CH5N, \qquad (R6)$$
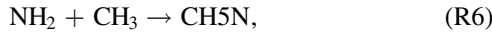
followed by photodissociation to form HCN,

$$CH_5N \xrightarrow{h\nu} HCN + 2H_2. \qquad (R7)$$
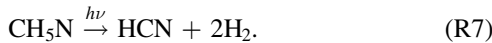
Reaction (R6) is the critical step in this HCN formation mechanism, and it requires the CH_3 radical to be available. The CH_3 in Reaction (R6) is mainly produced by

$$H + CH_4 \rightarrow H_2 + CH_3. \qquad (R8)$$
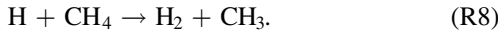
Note that the photodissociation of CH_4, which also produces CH_3, does not contribute significantly to the source of CH_3 in Reaction (R6) because the photodissociations of CH_4 and NH_3 typically occur at very different pressures. Another formational path of HCN is through

$$NH_2 + C_2H_3 \rightarrow C_2H_5N, \qquad (R9)$$

followed by photodissociation

$$C_2H_5N \xrightarrow{h\nu} HCN + CH_3 + H. \qquad (R10)$$
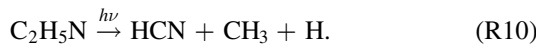
The C_2H_3 in Reaction (R9) is mainly produced by

$$H + C_2H_2 \xrightarrow{M} C_2H_3, \qquad (R11)$$
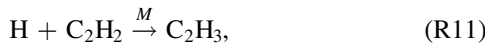
and C_2H_2 is ultimately produced by the photodissociation of CH_4 and then transported to the pressure of the photodissociation of NH_3. The HCN produced in Reactions (R7) and (R10) is photodissociated to form CN, but CN quickly reacts with H_2 and C_2H_2 to return to HCN. Thus, HCN does not have significant net chemical loss and is transported together with N_2 through the lower boundary.

The NH_3–CH_4 coupling (Reactions (R6)–(R8)) dominates the formation of HCN over the NH_3−C_2H_2 coupling (Reactions (R9)–(R11)) in temperate H_2-dominated atmospheres by several orders of magnitude. This is because the mixing ratio of C_2H_2 at the pressure of NH_3 photodissociation is typically very small on temperate planets like K2-18 b and PH2 b (Figures 6 and 7). On colder planets like Kepler-167 e, more C_2H_2 is

available and the NH_3−C_2H_2 coupling can contribute 1%–10% of the HCN formation, consistent with the results for Jupiter (Moses et al. 2010). We also note that past models of warm and hot H_2-rich exoplanets suggested different reactions to represent the NH_3−CH_4 coupling, including $NH + CH_3$ (Line et al. 2011) and $N + CH_3$ (Kawashima & Ikoma 2018; Hobbs et al. 2019); in our models the contribution from $N + CH_3 \rightarrow HCN + H_2$ contributes to the formation of HCN less than Reactions (R6)–(R8) by more than three orders of magnitude.

The efficacy of the NH_2 path to produce N_2 and HCN and the branching between N_2 and HCN depend on the abundance of H and the temperature. Reaction (R8) has an activation energy of $33.60 \text{ kJ mol}^{-1}$ (Baulch et al. 1992) and does not occur at very low temperatures. At the pressure of NH_3 photodissociation, the temperature is 220–240 K in K2-18 b and PH2 b, 120–130 K in Kepler-167 e, and $\sim$110 K in Jupiter. This makes Reaction (R8) faster by six orders of magnitude in K2-18 b and PH2 b than in Kepler-167 e or Jupiter, eventually leading to an efficient HCN production and a high abundance in the middle atmosphere. This is why the HCN production mechanism (Reactions (R6)–(R8)) does not operate efficiently in giant planets in the solar system but can build up HCN in warmer exoplanetary atmospheres.

The abundance of H is another important control. From Figure 11, we can see that a higher abundance of H would enhance the recycling from N_2H_4 to NH_2, produce more NH_3 to react with NH_2, and help the return of NH_2 to NH_3. In other words, a higher abundance of H would reduce the overall efficacy of the NH_2 path but favor the branch that leads to HCN. At the pressure of NH_3 photodissociation, the main source of H is the combination of Reactions (R1) and (R2), whose net result is the dissociation of H_2 but not NH_3. The sink of H is mainly Reaction (R3) and the direct recombination $H + H \xrightarrow{M} H_2$. In high-metallicity atmospheres, another sink of H is Reaction (R5) followed by

$$N_2H_4 + H \rightarrow N_2H_3 + H_2, \qquad (R12)$$

and

$$N_2H_3 + H \rightarrow 2NH_2. \qquad (R13)$$
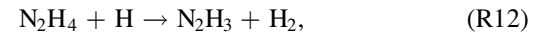
The net result of Reactions (R5), (R12), and (R13) is $H + H \rightarrow H_2$. Therefore, the chemical network that starts with the photodissociation of NH_3 is both a source and a sink of H, which feed back to determine the outcome of the network in a non-linear way. For example, the NH_2 channel is a minor pathway to form N_2 in the solar or $10 \times$ solar abundance atmosphere of K2-18 b, but it becomes an important pathway in the $100 \times$ solar atmosphere.

The abundance of H at the pressure of NH_3 photodissociation also explains the different sensitivity of the HCN mixing ratio on the inclusion of a deep-tropospheric source of CO/CO and a partial depletion of NH_3. For K2-18 b, the reduction in the HCN mixing ratio is small or proportional to the reduction in the input NH_3 abundance, but more reduction in the HCN mixing ratio is found for PH2 b (Figures 6 and 7). This is because the photodissociation of NH_3 occurs at higher pressures in PH2 b than in K2-18 b. When abundant CO exists, the reactions $CO + H \xrightarrow{M} HCO$ and $HCO + H \rightarrow CO + H_2$ efficiently remove H. Note that the first reaction in this cycle is three-body and only significant at sufficiently high pressures. This sink of H results in the reduction of CH_3 production
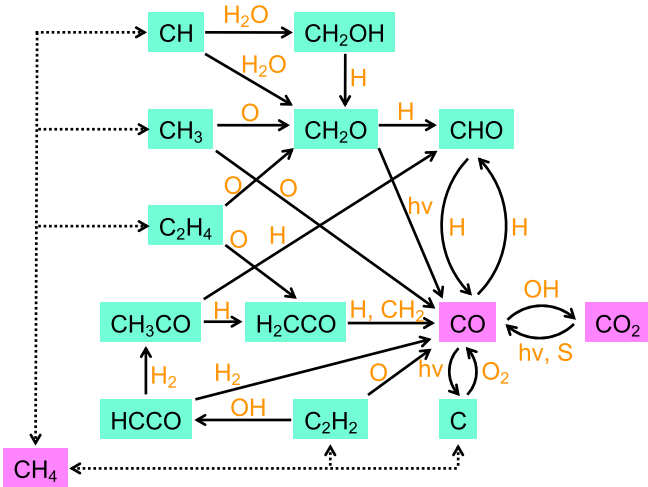
Figure 12. Chemical network from the photodissociations of CH_4 and H_2O in temperate/cold and H_2-dominated atmospheres. Not all reactions are shown, and the importance of the shown reactions changes from case to case. The dashed links represent the chemical network of CH_4 and hydrocarbons in cold and H_2-dominated atmospheres, as standard in the literature (e.g., Gladstone et al. 1996; Moses et al. 2005). The photodissociation of H_2O provides oxidizing radicals such as OH. When CH_4 is photodissociated together with H_2O, CO and CO_2 can be formed in addition to hydrocarbons.

(Reaction R8) and thus disfavors the branch in the NH_2 path that leads to HCN.

To summarize, the numerical models and the HCN formation mechanism presented here indicate that HCN and N_2 are generally the expected outcomes of the photodissociation of NH_3 in gaseous exoplanets that receive stellar irradiance approximately equal to Earth's, regardless of the stellar type.

3.4. Photolysis of CH_4 Together with H_2O

The formation of CO and CO_2 as the most abundant photochemical gases of carbon on K2-18 b and PH2 b is another significant finding of our numerical models. The photodissociation of CH_4 in colder H_2-dominated atmospheres —such as the giant planets' atmospheres in the solar system— produces hydrocarbons such as C_2H_6 and C_2H_2 but not oxygenated species (e.g., Gladstone et al. 1996; Moses et al. 2005). This is because H_2O condenses out and is almost completely removed from the above-cloud atmosphere (such as in Kepler-167 e, Figure 8). External sources such as comets and interplanetary dust can supply oxygen to the upper atmospheres of Jupiter and the other giant planets (e.g., Moses et al. 2005; Dobrijevic et al. 2020), but we do not include this source in the present study. For warmer planets, however, H_2O is only moderately depleted by condensation. The above-cloud water is photodissociated at approximately the same pressure as is CH_4 (Figures 6 and 7). The photodissociations of CH_4 and H_2O together in H_2-dominated atmospheres produce a chemical network beyond hydrocarbons (Figure 12) and eventually lead to the formation of CO and CO_2. Even warmer atmospheres (e.g., the atmosphere of GJ 1214b with an effective temperature of 500–600 K) may also have CO and CO_2 as the most abundant photochemical gases of carbon (e.g., Kempton et al. 2011; Kawashima & Ikoma 2018).

The photodissociation of CH_4 and the subsequent chemical reactions produce a wealth of hydrocarbons and radicals, and many of them (e.g., C, CH, CH_3, C_2H_2, and C_2H_4) lead to

chemical pathways that form CO (Figure 12). Between K2-18 b and PH2 b and among the modeled metallicities, we do not see a monotonic trend regarding the relative contribution of these CO forming pathways, probably due to many chemical cycles and feedback in hydrocarbon photochemistry. CO is converted to CO_2 by the reaction with OH:

$$CO + OH \rightarrow CO_2 + H. \qquad (R14)$$
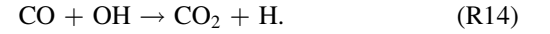
Reaction (R14) is the dominant source of CO_2 in all models, and the only significant chemical loss of CO_2 is to form CO via either photodissociation or the reaction with elemental sulfur when available (Figure 12). The CO_2 that is not returned to CO is then transported through the lower boundary.

What are the sources of OH, O, and H that power the chemical pathways shown in Figure 12? At the pressure of CH_4 and H_2O photodissociation, the source of OH is the photodissociation of water,

$$H_2O \xrightarrow{h\nu} H + OH, \qquad (R15)$$

and the main sink is the reaction with H_2,

$$OH + H_2 \rightarrow H_2O + H. \qquad (R16)$$
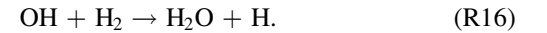
Reaction (R16) is the main sink of OH in all models, which means that the use of OH in the chemical pathways shown in Figure 12 does not usually become the dominant sink of OH. Reactions (R15) and (R16) together are equivalent to the net dissociation of H_2, which overtakes the photodissociation of CH_4 and subsequent hydrocarbon reactions as the dominant source of H in temperate atmospheres. Lastly, the main source of O is the photodissociation of CO and CO_2, which eventually traces to OH and the photodissociation of water.

At this point we can explain the ratio between CO_2 and CO in the middle atmosphere, which is ~ 1 on K2-18 b and ~ 10 on PH2 b (Figures 6 and 7). Because Reaction (R14) is the main source of CO_2 and photodissociation is the main sink, the number density of CO_2 is $\sim k_{R14}[CO][OH]/J_{CO_2}$, where k is the reaction rate constant and $[]$ means the number density of a molecule. Because Reaction (R15) is the main source of OH, the number density of OH is $\propto J_{H_2O}[H_2O]$. Therefore, the ratio between CO_2 and CO is $\propto J_{H_2O}[H_2O]/J_{CO_2}$. For any given metallicity, the abundance of H_2O in the middle atmosphere of PH2 b is $3\sim 5$-fold greater than that in K2-18 b because PH2 b is slightly warmer (Figures 6 and 7). And, J_{H_2O} at the top of the atmosphere on PH2 b is approximately twice that on K2-18 b, while J_{CO_2} is similar between the two planets (Figure 2). Together, this causes the $[CO_2]/[CO]$ ratio to be greater in the atmosphere of PH2 b than in K2-18 b by ~ 10-fold.

This trend to maintain the $[CO_2]/[CO]$ ratio also controls how the atmosphere reacts to a deep-tropospheric source of CO and CO_2 that is applied as input at the lower boundary. The input CO_2 is always less than CO by one or more orders of magnitude (Figures 3–5). On PH2 b, photochemical processes convert CO into CO_2 in the middle atmosphere ($\sim 10^2$ Pa), and cause the steady-state mixing ratio of CO_2 to be greater than that of CO. This conversion even becomes a significant sink of H_2O and causes H_2O to be depleted in the middle atmosphere in the $100\times$ solar metallicity case (Figure 7). The CO to CO_2 conversion is not so strong in the atmosphere of K2-18 b or Kepler-167 e, and their mixing ratios in the middle atmosphere are largely the input values at the lower boundary (Figure 6).

Finally, let us turn to the impact of H_2O and NH_3 photodissociation on the hydrocarbon chemistry. Compared with Kepler-167 e, the mixing ratio of C_2H_6—the dominant, supposedly long-lived hydrocarbon—in K2-18 b and PH2 b is smaller and sometimes features an additional peak near the cloud deck (Figures 6–8). Particularly, the atmospheres of K2-18 b and PH2 b have a strong sink of C_2H_6 at $\sim$1–10 Pa, while the atmosphere of Kepler-167 e does not. This sink is ultimately because of the high abundance of H produced by the photodissociation of H_2O (Reactions (R15) and (R16)). The detailed reaction path involves the formation of C_2H_5 from C_2H_6 (by direct reaction with H or photodissociation to form C_2H_4 followed by H addition), and then $C_2H_5 + H \rightarrow 2\,CH_3$. Because of the abundance of H, CH_3 mostly combines with H to form CH_4, rather than recombines to form C_2H_6. It is well known that the abundance of hydrocarbons is fundamentally controlled by the relative strength between $H + CH_3 \xrightarrow{M} CH_4$ and $CH_3 + CH_3 \xrightarrow{M} C_2H_6$ (e.g., Gladstone et al. 1996; Moses et al. 2005). Here, we find that the added H from H_2O photodissociation results in a net sink for C_2H_6 in K2-18 b and PH-2 b at $\sim$1–10 Pa and limits the abundance of hydrocarbons in their atmospheres. This sink does not exist in the atmosphere of Kepler-167 e, because little H_2O photodissociation occurs in its atmosphere. Additionally, near the cloud deck, the temperature is warmer, and Reaction (R8) that uses H from the photodissociation of NH_3 provides an additional source of CH_3, and some of the CH_3 becomes C_2H_6 and thus it peaks near the cloud deck. The formation of hydrocarbons is thus strongly impacted by the water and nitrogen photochemistry.

3.5. Spectral Features of H_2O, CH_4, NH_3, and Photochemical Gases

3.5.1. Transmission Spectra

Figures 13–15 show the transmission spectra of the temperate and cold planets K2-18 b, PH2 b, and Kepler-167 e, based on the gas and sulfur haze profiles simulated by the photochemical models. These modeled spectra can be regarded as the canonical examples of a temperate (Earth-like insolation) planet irradiated by an M dwarf star (K2-18 b, and also TOI-1231b), a temperate (Earth-like insolation) planet irradiated by a G/K star (PH2 b), and a cold ($\sim$0.1 × Earth insolation) planet irradiated by a G/K star (Kepler-167 e). Here, we focus on the wavelength range 0.5–5.0 μm, where several instruments on JWST will provide spectral capabilities (e.g., Beichman et al. 2014).

For K2-18 b, the equilibrium gases CH_4, H_2O, and NH_3, as well as the photochemical gas HCN have potentially detectable spectral features in the visible to mid-infrared wavelengths (Figure 13). Adding deep-tropospheric source of CO, CO_2, and N_2 and sink of NH_3 does not cause a significant change of the spectrum of a 10 × solar metallicity atmosphere. However, a 100 × solar metallicity atmosphere with deep-tropospheric source and sink would be free of the spectral features of NH_3 or HCN, but instead have potentially detectable features of CO_2 and CO.

Strikingly, the models from 1 × to 100 × solar abundance and with the standard eddy diffusion coefficient provide good fits to the existing transit depth measurements by K2, HST, and Spitzer (Benneke et al. 2019; Tsiaras et al. 2019). The models with a 100-fold greater eddy diffusion coefficient would have the sulfur haze layer extending to 10^2 Pa and mute the spectral

features in 1.1–1.7 μm, at odds with the HST data. Both CH_4 and H_2O contribute to the spectral modulations seen by HST, which may have caused the difficulties in the identification of the gases by spectral retrieval (Benneke et al. 2019; Tsiaras et al. 2019; Blain et al. 2021).

HCN, one of the most abundant photochemical gases in the middle atmosphere, is likely detectable in K2-18 b via its spectral band at $\sim$3.0 μm. The HCN is produced from the photodissociation of NH_3 in the presence of CH_4. Also at 3.0 μm are the absorption bands of NH_3 and to a lesser extent C_2H_2. It would be possible to disentangle these bands with a reasonably wide wavelength coverage because NH_3 has multiple and more prominent bands in the mid-infrared (Figure 13), and because C_2H_2 should have a minimal abundance in the middle atmosphere (Figure 6) and contribute little to the transmission spectra.

The spectral bands of CO_2 and CO can be seen in the modeled spectra (in 4–5 μm) of K2-18 b only when the atmosphere has supersolar metallicity and the transport from the deep troposphere is taken into account (Figure 13). In other words, the CO and CO_2 that are produced from the photodissociation of CH_4 together with H_2O would have too low mixing ratios to be detected. The photodissociation of CH_4 also produces C_2H_6. While C_2H_6 has strong bands at 3.35 and 12 μm, they would not be detectable due to its relatively low abundance and the strong CH_4 and NH_3 bands at the same wavelength, respectively (Figure 13).

For PH2 b, prominent spectral bands of CH_4, H_2O, and the photochemical gases CO_2 and HCN can be expected (Figure 14). NH_3 is not detectable because it is depleted by photodissociation to the cloud deck (Figure 7). Even though its pressure of photochemical depletion can be reduced to $\sim$10^2 Pa for a large eddy diffusion coefficient, the sulfur haze in that case would mute spectral features that are generated from approximately the same pressure levels (Figure 10) and thus cause NH_3 to be undetectable. HCN, CO_2, and CO are the most abundant photochemical gases (Figure 7); but the CO bands are intrinsically weaker and so CO_2 and HCN are the detectable photochemical gases via their spectral bands at 4.2 and 3.0 μm, respectively. Similar to K2-18 b, adding a deep-tropospheric source of CO, CO_2, and N_2 and sink of NH_3 does not cause a significant change of the spectrum of a 10 × solar metallicity atmosphere. However, a 100 × solar metallicity atmosphere with a deep-tropospheric source and sink would not have the spectral features of H_2O or HCN and would have more prominent features of CO_2 and CO, as predicted by the photochemical model (Figure 7).

Lastly for the cold planet Kepler-167 e, the transmission spectra will be dominated by the absorption bands of CH_4 (Figure 15), as H_2O is completely removed by condensation and NH_3 by condensation and photodissociation. For a large eddy diffusion coefficient, the pressure of photochemical depletion of NH_3 can be reduced to $\sim$10^3 Pa (Figure 10) and this can produce a spectral band of NH_3 at $\sim$3.0 μm. Thus, a search for this absorption band in the transmission spectra may constrain the eddy diffusion coefficient, although to distinguish it with a small peak due to the combined absorption of the photochemical gases HCN and C_2H_2 (Figure 15) may involve quantification through photochemical models. The main photochemical gas in this cold atmosphere C_2H_6 has spectral bands at 3.35 and 12 μm. The 3.35 μm band is buried by a strong CH_4 band, and while not shown in Figure 15, the 12 μm
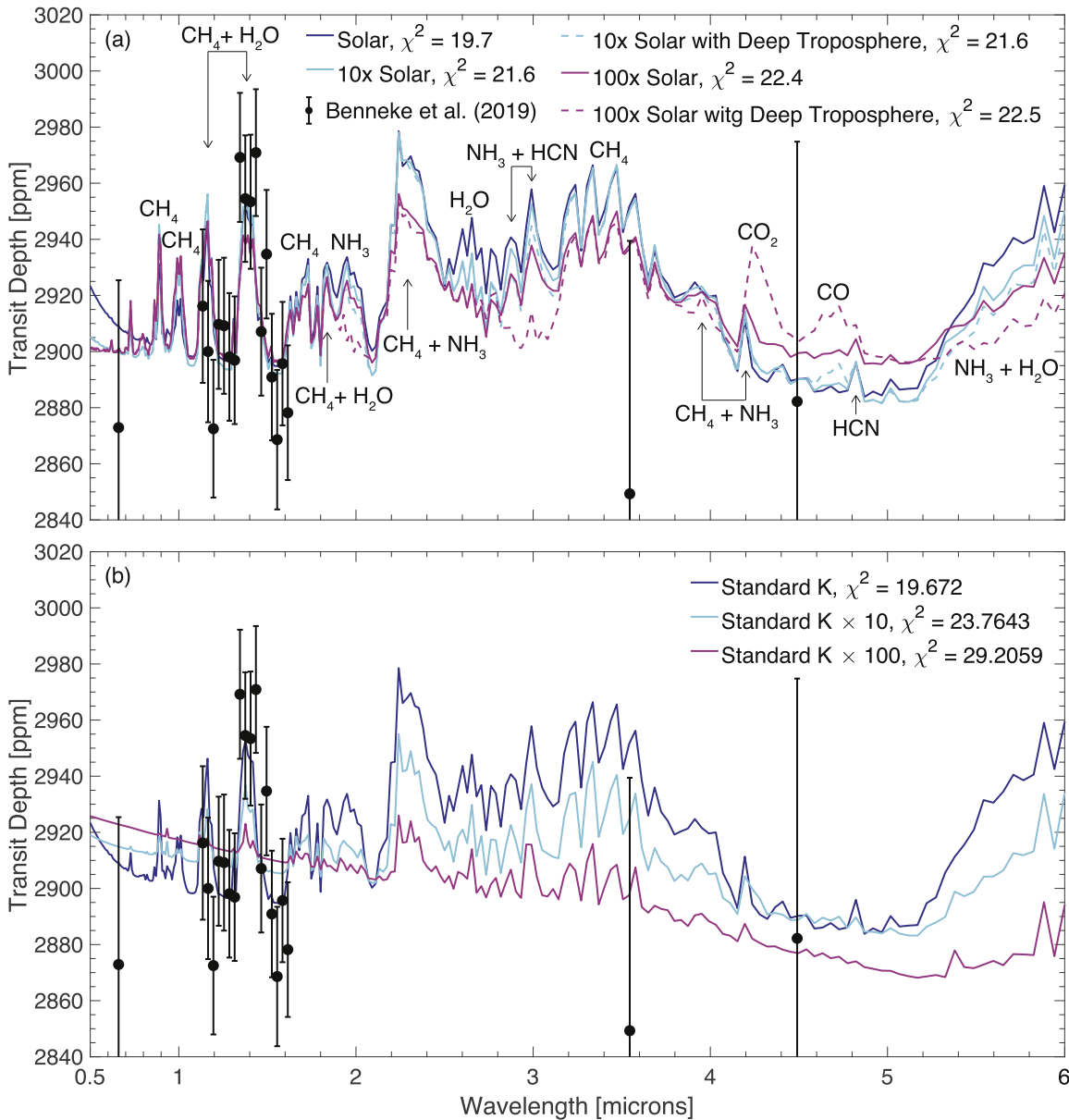
Figure 13. Modeled transmission spectra of the temperate sub-Neptune K2-18 b for varied metallicities (a) and varied eddy diffusion coefficients at solar metallicity (b). The dashed lines show model spectra with a deep-tropospheric source of CO, CO_2, and N_2 and sink of NH_3. All models with the standard eddy diffusion coefficient fit the observed transit depths. The equilibrium gases (CH_4, H_2O, and NH_3) and the photochemical gas HCN are detectable in the wavelength range 0.5–5.0 μm. The 100 × solar metallicity atmosphere with a deep-tropospheric source and sink can have detectable features of CO_2 and CO.

band might be detectable given appropriate instrumentation with the spectral capability in the corresponding wavelength range. Finally, the deep-troposphere-sourced CO_2 and CO in a 100 × solar metallicity atmosphere may produce detectable spectral features at 4–5 μm.

To summarize, transmission spectroscopy from the visible to mid-infrared wavelengths can provide the sensitivity to detect the equilibrium gases CH_4 and H_2O, and the photochemical gases HCN, and in some cases CO_2 in temperate/cold and H_2-rich exoplanets. We do not expect C_2H_6 to be detectable. NH_3 would be detectable on temperate planets around M dwarf stars but not detectable on temperate planets around G/K stars. The deep-tropospheric source and sink can have a major impact only on the transmission spectrum of a 100 × solar metallicity atmosphere, where typically the features of NH_3 and HCN would be reduced and those of CO_2 and CO would be

amplified. The detection and nondetection of these gases will thus test the photochemical model and improve our understanding of the photochemical mechanisms as well as tropospheric transport in temperate/cold and H_2-dominated atmospheres.

3.5.2. Spectra of the Reflected Starlight

The temperate and cold planets around G/K stars are widely separated from their host stars and may thus also be characterized in the reflected starlight by direct imaging. Figure 16 shows the geometric albedo spectra of PH2 b and Kepler-167 e in the visible and near-infrared wavelengths that approximately correspond to the Roman Space Telescope's coronagraph instrument (Kasdin et al. 2020) and its potential Starshade Rendezvous (Seager et al. 2019) and the HabEx
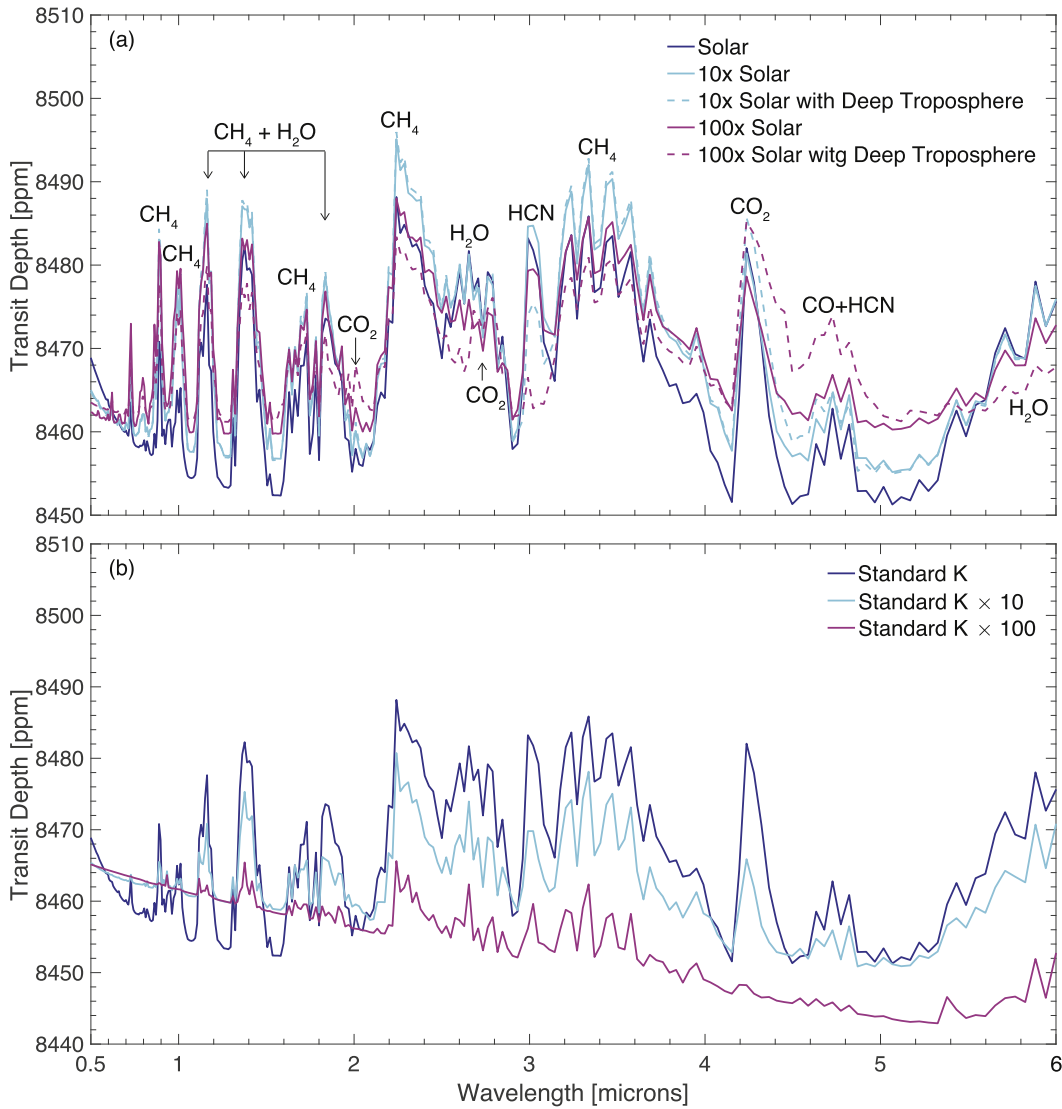
Figure 14. Modeled transmission spectra of the temperate gas giant PH2 b for varied metallicities (a) and varied eddy diffusion coefficients at solar metallicity (b). The dashed lines show model spectra with a deep-tropospheric source of CO, CO_2, and N_2 and sink of NH_3. Several equilibrium gases (CH_4 and H_2O) and photochemical gases (HCN, CO_2, and CO) are detectable in the wavelength range 0.5–5.0 μm.

concept (Gaudi et al. 2020). While PH2 b and Kepler-167 e themselves are not potential targets for these missions, their albedo spectra broadly resemble the targets in the temperate (PH2 b) and cold (Kepler-167 e) regimes.

The spectral features of CH_4 and H_2O can be seen in the reflected starlight of PH2 b. This ability to detect H_2O in giant planets warmer than Jupiter is consistent with the finding of MacDonald et al. (2018). In addition to the absorption features of CH_4 and H_2O, the albedo spectra of PH2 b feature the absorption of the sulfur (S_8) haze layer at wavelengths shorter than $\sim$0.5 μm. This result is consistent with the findings of Gao et al. (2017). For a greater eddy diffusion coefficient, the sulfur haze layer is higher and the spectral features of CH_4 and H_2O become weaker. Interestingly, the absorption features of H_2O are the most prominent in the solar abundance case, and they are somewhat swamped by the adjacent CH_4 features at higher metallicities. This is because, as H_2O condenses out, the above-cloud mixing ratio of H_2O only slightly increases with the metallicity, while that of CH_4 increases proportionally (Figure 7). Only the absorption of CH_4 can be seen in the

albedo spectra of Kepler-167 e, as H_2O is depleted by condensation. On both planets, the spectral features of NH_3 are not seen due to its weak absorption (Irwin et al. 2018) and photochemical depletion to the cloud deck (Figures 7 and 8). The deep-tropospheric source and sink has minimal impact on the albedo spectra, unless in the $100 \times$ solar metallicity atmosphere on PH2 b where a reduction of the CH_4 features can be seen.

4. Discussion

The results and analyses presented in Section 3 indicate that the temperate and H_2-rich exoplanets, particularly those orbiting M dwarf stars, provide an unprecedented opportunity to characterize the photochemical mechanisms in low-temperature atmospheres. So far, these planets include K2-18 b, TOI-1231 b, and LHS-1140 b if they have H_2-dominated atmospheres. H_2-dominated atmospheres that receive stellar irradiation equal to that of Earth are not found in the solar system, and we have shown here that this unique exoplanetary regime would result in mechanisms to form HCN as a uniformly
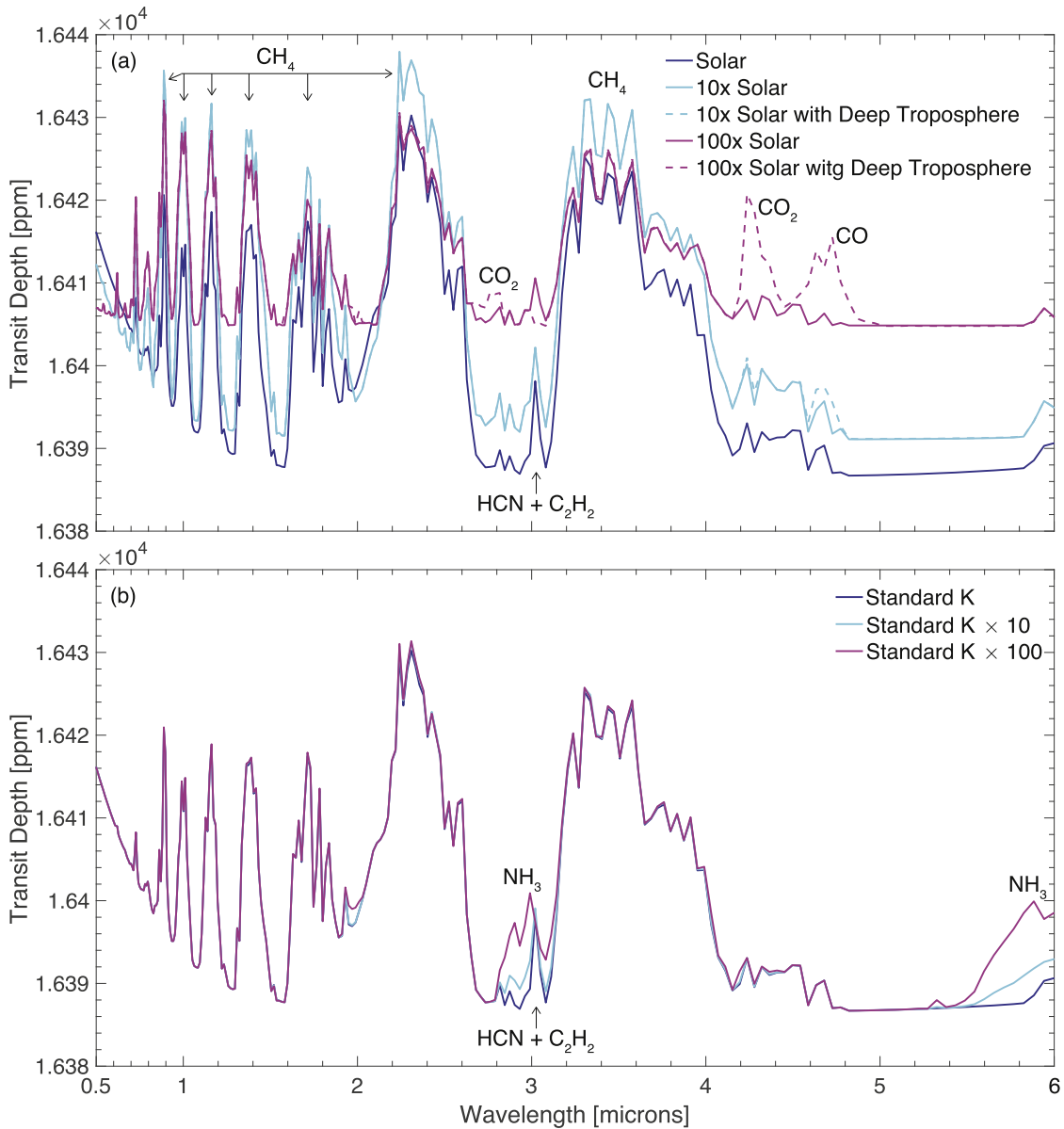
Figure 15. Modeled transmission spectra of the cold gas giant Kepler-167 e for varied metallicities (a) and varied eddy diffusion coefficients at solar metallicity (b). The dashed lines show model spectra with a deep-tropospheric source of CO, CO_2, and N_2 and sink of NH_3. With the standard eddy diffusion coefficient, CH_4 is the only detectable equilibrium gas and the photochemical gases HCN and C_2H_2 result in a small peak at ~ 3 μm. The $100 \times$ solar metallicity atmosphere with a deep-tropospheric source and sink can have detectable features of CO_2 and CO. Greater eddy diffusion coefficients can produce potentially detectable NH_3.

abundant product from the photodissociation of NH_3 in presence of CH_4, as well as detectable levels of CO_2 on planets around G/K stars from the photodissociation of CH_4 together with H_2O. The observations of temperate and H_2-rich exoplanets thus promise to greatly expand the types of molecules detected in exoplanet atmospheres. Interestingly, HCN is one of the most important molecules for prebiotic chemistry (e.g., Patel et al. 2015), and the exoplanet observations may constrain the photochemical pathways for its formation in primordial planetary atmospheres.

For K2-18 b, our model predicts that the spectral features of CH_4 can have a size of ~ 80 ppm in the transit depth, and those of H_2O, NH_3, HCN, and CO_2 (from the deep troposphere) would have a size of $30 \sim 60$ ppm. These quantities are substantially above the current estimate of the potential "noise floor" of the near-infrared instruments on JWST ($< \sim 10$ ppm;

Schlawin et al. 2020, 2021), and are thus likely measurable. These spectral features may also be within the reach of ARIEL (Tinetti et al. 2018; Changeat et al. 2020).

An an example, we have used PandExo (Batalha et al. 2017) to estimate the overall photometric uncertainties achieved by observing the transits of K2-18 b with the G235H and G395H gratings of the NIRSpec instrument on JWST. These two channels would cover the wavelength range 1.7–5.2 μm and thus provide the sensitivity to the spectral features shown in Figure 13. We find that with two visits in G235H and four visits in G395H, the overall photometric precision would be ~ 20 ppm per spectral element at the resolution of $R = 100$ in both wavelength channels, and this precision should enable the detection of CH_4, H_2O, NH_3, the photochemical gas HCN, and possibly CO_2. If the spectral resolution is reduced to $R = 50$, the number of visits could be halved, but this could cause
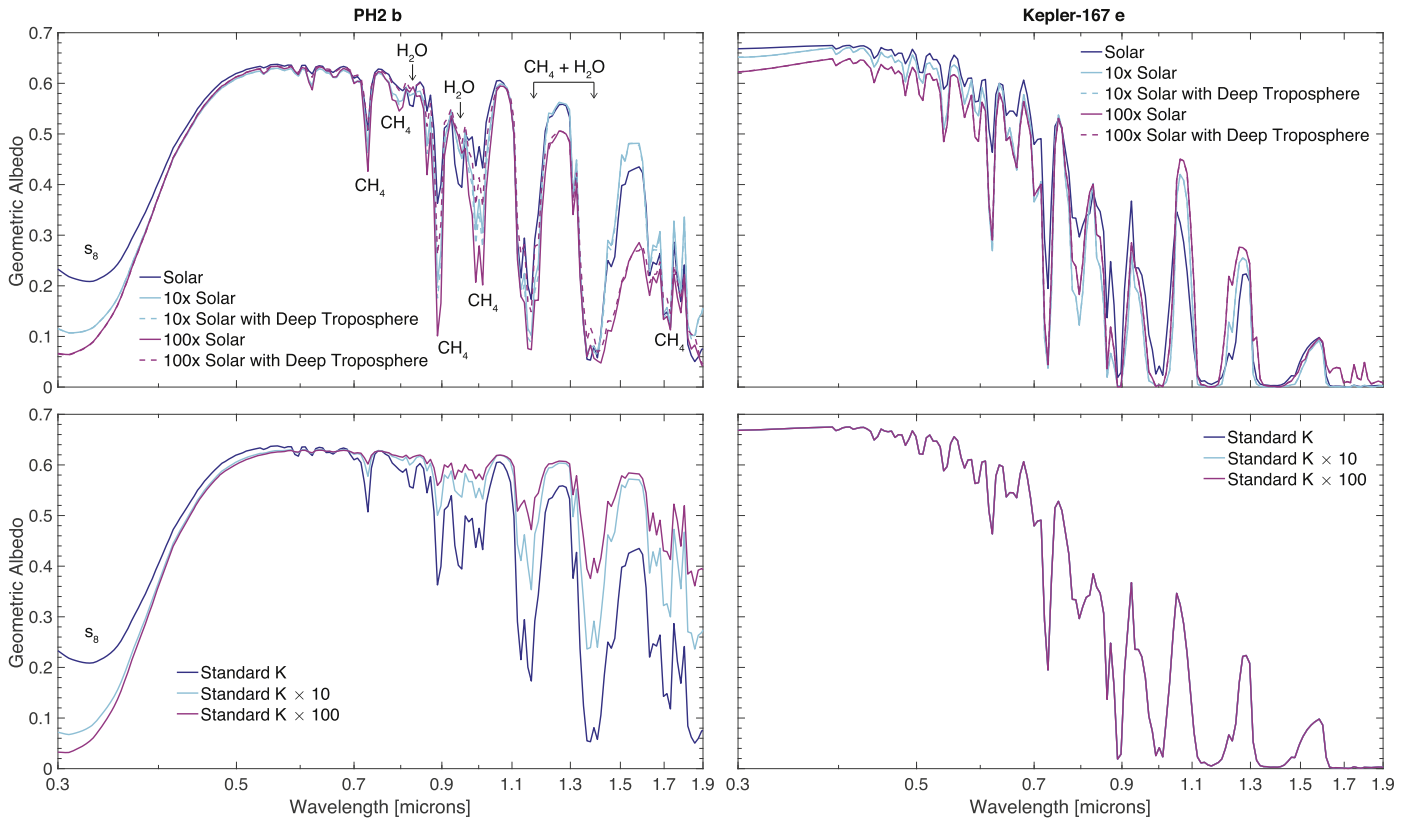
Figure 16. Modeled geometric albedo spectra of the temperate gas giants PH2 b and the cold gas giant Kepler-167 e for varied metallicities and varied eddy diffusion coefficients at solar metallicity. The dashed lines show model spectra with a deep-tropospheric source of CO, CO_2, and N_2 and sink of NH_3. All absorption features in Kepler-167 e's spectra are due to CH_4. Both H_2O and CH_4 can be detectable in the reflected starlight of PH2 b and only CH_4 can be detectable in Kepler-167 e.

spectral ambiguity between NH_3 and HCN because they both have absorption bands at $\sim 3.0\ \mu m$ (Figure 13). Spectral ambiguity in the transmission spectra with a resolution of $R \sim 50$ or less has been recently shown with HST at 1.1–$1.7\ \mu m$ (Mikal-Evans et al. 2020).

The size of the transmission spectral features expected for temperate and cold gas giants around G/K stars, such as PH2 b and Kepler-167 e, is small but probably not prohibitive. For example, our model predicts that the spectral features of CH_4 can have a size of ~ 50 ppm in the transit depth, and those of H_2O, CO_2, and HCN would have a size of $20 \sim 30$ ppm. Several visits may need to be combined to achieve the photometric precision to detect these gases. Complementary to transmission spectroscopy, future direct-imaging missions can readily detect CH_4, H_2O, and clouds (e.g., Damiano & Hu 2020), as well as the sulfur haze produced by atmospheric photochemistry.

While we focus on temperate and cold planets in this paper, the photochemical mechanisms and the predictions on the gas formation and spectral features should remain applicable to the planets that are only slightly warmer than K2-18 b and PH2 b. This is because the results on these planets do not rely on the formation of water clouds. We suspect that the results should be applicable as long as the dominant O, C, N, and S species in thermochemical equilibrium with H_2 are H_2O, CH_4, NH_3, and H_2S, and the assumptions on other atmospheric parameters (e.g., the eddy diffusion coefficient) remain broadly valid.

The eddy diffusion coefficient adopted in this work corresponds to that of Jupiter (Conrath & Gierasch 1984) and features a minimum at the bottom of the stratosphere. This minimum value is also close to the eddy diffusion coefficient at the troposphere−stratosphere boundary of Earth's atmosphere (Massie & Hunten 1981). However, the adopted eddy diffusion coefficient at the bottom of the stratosphere is smaller than the values used in past photochemical models of warmer exoplanets (e.g., GJ 1214 b and GJ 436 b; Kempton et al. 2011; Moses et al. 2013; Hu & Seager 2014) or the values derived from a 3D particulate tracer-transport model conditioned on hot Jupiters (Parmentier et al. 2013) by several orders of magnitude. We note that Earth, the cold giant planets in the solar system, and the modeled K2-18 b (Blain et al. 2021; Charnay et al. 2021) all have a temperature inversion and are thus true stratospheres, while atmosphere models of the warm exoplanets GJ 1214 b and GJ 436 b do not predict a temperature inversion (e.g., Kempton et al. 2011; Moses et al. 2013). The lower temperature and the temperature inversion may both contribute to the lower eddy diffusion coefficient on temperate and cold exoplanets. Predictive models of the eddy diffusion coefficient in exoplanets are being developed (e.g., Zhang & Showman 2018a, 2018b) and can be tested by future observations as shown in Figures 13–15.

We have also shown in Section 3 that the deep-tropospheric source of CO, CO_2, and N_2 and sink of NH_3 can substantially change the composition of the observable part of the atmosphere—and the transmission spectrum—if the atmosphere has $100 \times$ solar metallicity. The main change is the reduction of NH_3 and HCN and the enhancement of CO and CO_2 in the spectrum. As such, detecting and measuring the abundance of these gases in the temperate H_2-dominated atmosphere may provide constraints on the temperature and the

strength of vertical mixing in the deep troposphere (e.g., Fortney et al. 2020). One should note that modification of the deep-tropospheric abundance of gases by photochemical processes will be important in this endeavor: NH_3 is expected to be depleted anyway and CO_2 should overtake CO as the main carbon molecule in the middle atmosphere of temperate and H_2-rich exoplanets of G/K stars.

A recently published study of atmospheric photochemistry in the atmosphere of K2-18 b (Yu et al. 2021) came to our notice during the peer-review phase of this work. The "no-surface" case in Yu et al. (2021) has a comparable physical picture as the $100 \times$ solar metallicity case with the deep-tropospheric source and sink presented in Figure 6. A common feature is that such an atmosphere would be rich in CO and CO_2, and the difference in the profiles of HCN and other photochemical gases between the models may be due to the assumed profile of eddy diffusivity.

Lastly, we emphasize that several effects of potential importance have not been studied in this work. A more accurate pressure–temperature profile from 1D or 3D models may improve the prediction on the extent of water vapor depletion by condensation. A temperature inversion would result in higher temperatures in the upper stratosphere than what has been adopted here, and this may have an impact on the efficacy and relative importance of chemical pathways. A more accurate pressure–temperature profile and vertical mixing modeling for the deep troposphere may improve the prediction and perhaps remove the need for the endmember scenarios as presented. On planets that are expected to be tidally locked, the transmission spectra are controlled by the chemical abundance at the limb (e.g., Steinrueck et al. 2019; Drummond et al. 2020), and thus the horizontal transport of long-lived photochemical gases such as HCN and CO_2 may be important. Finally, we have not included hydrocarbon haze in this study, though it can form with both C_2H_2 and HCN in the atmosphere (Kawashima et al. 2019). We hope that the present work will help motivate future studies to address these potential effects.

5. Conclusion

We have studied the photochemical mechanisms in temperate/cold and H_2-rich exoplanets. For the H_2-rich planets (giants and mini-Neptunes) that receive stellar irradiance of approximately Earth's, we find that the main photochemical gases are HCN and N_2. The synthesis of HCN requires the photodissociation of NH_3 in the presence of CH_4 at a temperature $> \sim 200$ K. NH_3 is dissociated near the water cloud deck and thus has a minimal mixing ratio in the middle atmosphere (10–10^3 Pa) if the planet orbits a G/K star, but NH_3 can remain intact in the middle atmosphere if the planet orbits an M star. Additional photochemical gases include CO, CO_2, C_2H_6, and C_2H_2. CO and CO_2 are the main photochemical gas of carbon because of the photodissociation of H_2O together with CH_4. The photodissociation of H_2O also strongly limits the abundance of photochemical hydrocarbons in the atmosphere. For the planets that receive stellar irradiance of approximately $0.1 \times$ Earth's, the formation of HCN is limited by the low temperature, CO_2 or CO is not produced due to the nearly complete removal of H_2O by condensation, and the main photochemical gases are C_2H_6 and C_2H_2.

The photochemical models of the temperate sub-Neptune K2-18 b assuming 1–$100 \times$ solar abundances result in transmission spectra that fit the current measurements from K2,

HST, and Spitzer. Both CH_4 and H_2O contribute to the spectral modulation seen by HST. Transmission spectroscopy with JWST and ARIEL will likely provide the sensitivity to detect the equilibrium gases CH_4, H_2O, and NH_3, the photochemical gas HCN, and in some cases CO_2. C_2H_6 is unlikely to be detectable due to its low mixing ratio and spectral feature overwhelmed by CH_4. Transmission spectroscopy of the temperate giant planets around G/K stars will likely provide the sensitivity to detect CH_4, H_2O, and the photochemical gases HCN and CO_2, complementing future spectroscopy in the reflected light by direct imaging. If the eddy diffusion coefficient is greater than that in Jupiter by two orders of magnitude, the sulfur haze layer would subdue the transmission spectral features—but this situation is unlikely for K2-18 b because of the detected spectral modulation. These results are also applicable to similarly irradiated H_2-rich exoplanets, including TOI-1231 b and LHS-1140 b if they have H_2-dominated atmospheres.

The results here indicate that the temperate/cold and H_2-rich exoplanets, which often represent a temperature and atmospheric composition regime that is not found in the solar system, likely have rich chemistry above clouds that leads to a potpourri of photochemical gases, some of which will build up to the abundance detectable by transmission spectroscopy soon. The detection of atmospheric photochemical products in K2-18 b and other temperate exoplanets would expand the types of molecules detected in exoplanet atmospheres and greatly advance our understanding of the photochemical processes at works in low-temperature exoplanets.

ORCID iDs

Renyu Hu ⓘ https://orcid.org/0000-0003-2215-8485

References

Agúndez, M., Venot, O., Selsis, F., & Iro, N. 2014, ApJ, 781, 68
Airapetian, V., Glocer, A., Gronoff, G., Hebrard, E., & Danchi, W. 2016, NatGe, 9, 452
Atreya, S., & Romani, P. 1985, Recent Advances in Planetary Meteorology (Cambridge: Cambridge Univ. Press), 17
Atreya, S. K., Donahue, T. M., & Kuhn, W. R. 1977, Icar, 31, 348
Atreya, S. K., Wong, M. H., Owen, T. C., et al. 1999, P&SS, 47, 1243
Barclay, T., Pepper, J., & Quintana, E. V. 2018, ApJS, 239, 2
Batalha, N. E., Mandell, A., Pontoppidan, K., et al. 2017, PASP, 129, 064501
Baulch, D., Cobos, C., Cox, R., et al. 1992, JPCRD, 21, 411
Beichman, C., Benneke, B., Knutson, H., et al. 2014, PASP, 126, 1134
Benneke, B., Wong, I., Piaulet, C., et al. 2019, ApJL, 887, L14
Berger, T. A., Huber, D., Gaidos, E., & van Saders, J. L. 2018, ApJ, 866, 99
Blain, D., Charnay, B., & Bézard, B. 2021, A&A, 646, A15
Blumenthal, S. D., Mandell, A. M., Hébrard, E., et al. 2018, ApJ, 853, 138
Burrows, A., Hubbard, W. B., Lunine, J., & Liebert, J. 2001, RvMP, 73, 719
Burrows, A., & Sharp, C. 1999, ApJ, 512, 843
Burt, J. A., Dragomir, D., Mollière, P., et al. 2021, AJ, 162, 87
Changeat, Q., Edwards, B., Al-Refaie, A. F., et al. 2020, arXiv:2003.01486
Charnay, B., Blain, D., Bézard, B., et al. 2021, A&A, 646, A171

Cloutier, R., Astudillo-Defru, N., Doyon, R., et al. 2019, A&A, 621, A49
Conrath, B. J., & Gierasch, P. J. 1984, Icar, 57, 184
Damiano, M., & Hu, R. 2020, AJ, 159, 175
Davis, G., Naylor, D., Griffin, M. J., Clark, T., & Holland, W. S. 1997, Icar, 130, 387
De Pater, I., Romani, P. N., & Atreya, S. K. 1989, Icar, 82, 288
De Wit, J., Wakeford, H. R., Lewis, N. K., et al. 2018, NatAs, 2, 214
Dobrijevic, M., Loison, J., Hue, V., Cavalié, T., & Hickson, K. 2020, Icar, 335, 113375
dos Santos, L. A., Ehrenreich, D., Bourrier, V., et al. 2020, A&A, 634, L4
Drummond, B., Hébrard, E., Mayne, N. J., et al. 2020, A&A, 636, A68
Fegley, B., Jr., & Lodders, K. 1996, ApJL, 472, L37
Fortney, J. J., Mordasini, C., Nettelmann, N., et al. 2013, ApJ, 775, 80
Fortney, J. J., Visscher, C., Marley, M. S., et al. 2020, AJ, 160, 288
France, K., Loyd, R. P., Youngblood, A., et al. 2016, ApJ, 820, 89
Gao, P., Marley, M. S., Zahnle, K., Robinson, T. D., & Lewis, N. K. 2017, AJ, 153, 139
Gaudi, B. S., Seager, S., Mennesson, B., et al. 2020, arXiv:2001.06683
Gierasch, P., & Conrath, B. 1985, Recent Advances in Planetary Meteorology (Cambridge: Cambridge Univ. Press), 121
Gladstone, G. R., Allen, M., & Yung, Y. 1996, Icar, 119, 1
Heng, K., & Tsai, S.-M. 2016, ApJ, 829, 104
Hobbs, R., Shortle, O., Madhusudhan, N., & Rimmer, P. 2019, MNRAS, 487, 2242
Hu, R. 2019, ApJ, 887, 166
Hu, R., & Seager, S. 2014, ApJ, 784, 63
Hu, R., Seager, S., & Bains, W. 2012, ApJ, 761, 166
Hu, R., Seager, S., & Bains, W. 2013, ApJ, 769, 6
Irwin, P. G., Bowles, N., Braude, A. S., Garland, R., & Calcutt, S. 2018, Icar, 302, 426
Kasdin, N. J., Bailey, V., Mennesson, B., et al. 2020, Proc. SPIE, 11443, 114431U
Kawashima, Y., Hu, R., & Ikoma, M. 2019, ApJL, 876, L5
Kawashima, Y., & Ikoma, M. 2018, ApJ, 853, 7
Kaye, J. A., & Strobel, D. F. 1983a, Icar, 55, 399
Kaye, J. A., & Strobel, D. F. 1983b, Icar, 54, 417
Kempton, E. M.-R., Zahnle, K., & Fortney, J. J. 2011, ApJ, 745, 3
Kipping, D. M., Torres, G., Henze, C., et al. 2016, ApJ, 820, 112
Krasnopolsky, V. A. 2009, Icar, 201, 226
Krasnopolsky, V. A. 2014, Icar, 236, 83
Läuter, A., Lee, K., Jung, K., et al. 2002, CPL, 358, 314
Lavvas, P., Coustenis, A., & Vardavas, I. 2008, P&SS, 56, 67
Lavvas, P., Koskinen, T., Steinrueck, M. E., Muñoz, A. G., & Showman, A. P. 2019, ApJ, 878, 118
Lewis, J. S. 1969, Icar, 10, 365
Lindzen, R. S. 1981, JGRC, 86, 9707
Line, M. R., Vasisht, G., Chen, P., Angerhausen, D., & Yung, Y. L. 2011, ApJ, 738, 32
MacDonald, R. J., Marley, M. S., Fortney, J. J., & Lewis, N. K. 2018, ApJ, 858, 69
Madhusudhan, N., Nixon, M. C., Welbanks, L., Piette, A. A., & Booth, R. A. 2020, ApJL, 891, L7
Martonchik, J. V., Orton, G. S., & Appleby, J. F. 1984, ApOpt, 23, 541
Massie, S., & Hunten, D. 1981, JGRC, 86, 9859

Mikal-Evans, T., Crossfield, I. J., Benneke, B., et al. 2020, AJ, 161, 18
Molaverdikhani, K., Henning, T., & Mollière, P. 2019, ApJ, 883, 194
Mollière, P., van Boekel, R., Dullemond, C., Henning, T., & Mordasini, C. 2015, ApJ, 813, 47
Morley, C. V., Marley, M. S., Fortney, J. J., et al. 2014, ApJ, 787, 78
Morrissey, P. F., Feldman, P. D., McGrath, M. A., Wolven, B. C., & Moos, H. W. 1995, ApJL, 454, L65
Moses, J., Fouchet, T., Bézard, B., et al. 2005, JGRE, 110, E08001
Moses, J. I., Line, M. R., Visscher, C., et al. 2013, ApJ, 777, 34
Moses, J. I., Madhusudhan, N., Visscher, C., & Freedman, R. S. 2013, ApJ, 763, 25
Moses, J. I., Marley, M. S., Zahnle, K., et al. 2016, ApJ, 829, 66
Moses, J. I., Visscher, C., Fortney, J. J., et al. 2011, ApJ, 737, 15
Moses, J. I., Visscher, C., Keane, T. C., & Sperier, A. 2010, FaDi, 147, 103
Palmer, K. F., & Williams, D. 1974, JOSA, 64, 1107
Parmentier, V., Showman, A. P., & Lian, Y. 2013, A&A, 558, A91
Patel, B. H., Percivalle, C., Ritson, D. J., Duffy, C. D., & Sutherland, J. D. 2015, NatCh, 7, 301
Perry, R., & Green, D. 2007, Perry's Chemical Engineers' Handbook (8th ed.; New York: McGraw-Hill)
Piette, A. A., & Madhusudhan, N. 2020, ApJ, 904, 154
Ranjan, S., Schwieterman, E. W., Harman, C., et al. 2020, ApJ, 896, 148
Rimmer, P. B., & Rugheimer, S. 2019, Icar, 329, 124
Romani, P. N., De Pater, I., & Atreya, S. K. 1989, GeoRL, 16, 933
Schlawin, E., Leisenring, J., McElwain, M. W., et al. 2021, AJ, 161, 115
Schlawin, E., Leisenring, J., Misselt, K., et al. 2020, AJ, 160, 231
Seager, S., Kasdin, N. J., Booth, J., et al. 2019, BAAS, 51, 106
Seiff, A., Kirk, D. B., Knight, T. C., et al. 1998, JGRE, 103, 22857
Simon-Miller, A. A., Conrath, B. J., Gierasch, P. J., et al. 2006, Icar, 180, 98
Steinrueck, M. E., Parmentier, V., Showman, A. P., Lothringer, J. D., & Lupu, R. E. 2019, ApJ, 880, 14
Strobel, D. F. 1973, JAtS, 30, 1205
Thorngren, D. P., Fortney, J. J., Murray-Clay, R. A., & Lopez, E. D. 2016, ApJ, 831, 64
Tinetti, G., Drossart, P., Eccleston, P., et al. 2018, ExA, 46, 135
Tsai, S.-M., Kitzmann, D., Lyons, J. R., et al. 2018, ApJ, 862, 31
Tsiaras, A., Waldmann, I. P., Tinetti, G., Tennyson, J., & Yurchenko, S. N. 2019, NatAs, 3, 1086
Venot, O., Hébrard, E., Agúndez, M., et al. 2012, A&A, 546, A43
Visscher, C., & Moses, J. I. 2011, ApJ, 738, 72
Visscher, C., Moses, J. I., & Saslow, S. A. 2010, Icar, 209, 602
Vuitton, V., Yelle, R., Klippenstein, S., Hörst, S., & Lavvas, P. 2019, Icar, 324, 120
Waite, J., Cravens, T., Kozyra, J., et al. 1983, JGRA, 88, 6143
Wang, J., Fischer, D. A., Barclay, T., et al. 2013, ApJ, 776, 10
Woitke, P., Herbort, O., Helling, C., et al. 2021, A&A, 646, A43
Yelle, R. V., Griffith, C. A., & Young, L. A. 2001, Icar, 152, 331
Yu, X., Moses, J. I., Fortney, J. J., & Zhang, X. 2021, ApJ, 914, 38
Yung, Y. L., Allen, M., & Pinto, J. P. 1984, ApJS, 55, 465
Zahnle, K., Marley, M. S., Morley, C. V., & Moses, J. I. 2016, ApJ, 824, 137
Zahnle, K. J., & Marley, M. S. 2014, ApJ, 797, 41
Zhang, X., & Showman, A. P. 2018a, ApJ, 866, 1
Zhang, X., & Showman, A. P. 2018b, ApJ, 866, 2
Zhang, Z., Zhou, Y., Rackham, B. V., & Apai, D. 2018, AJ, 156, 178